GIANTS

Simulation Environment & Integration

Deliverable Number	D4.2
Deliverable Type	R – Document, Report
Dissemination Level	PU (Public)
Deliverable Responsible	KU Leuven
Planned Delivery Date	2025-03-31
Actual Delivery Date	2025-06-30
Document Version & Status	v1.6 | Final

Project Acronym	GIANTS
Project Title	Green Intelligent Affordable New Transport Solutions
Grant Agreement Number	101138220
Project Coordinator	Virtual Vehicle Research GmbH
Project Website	www.giants-project.eu

Funded by the European Union

GIANTS has received funding from the European Union's Horizon Europe research and innovation programme under Grant Agreement No. 101138220.

Author(s)

Name	Organisation	Name	Organisation
Tobias Lorscheider	VIF	Rastislav Toman	CVUT
Dionysios Panagiotopoulos	KUL	Felix Tischer	VIF
Christophe Langlois	KUL		

Reviewers

Name	Organisation	Date
Anoop Manappattu Vasudevan	Renault	2025-06-29
Kirill Khruntsov	TUX	2025-06-27

Change History

Version	Date	Name/Organisation	Description
v1.0	2025-05-26	Nicola Contartese/VIF	Structure, general input
v1.1	2025-06-11	Tobias Lorscheider/VIF	Added input chapter 3.3 and 3.4
v1.2	2025-06-19	Christophe Langlois, Dionysios Panagiotopoulos / KUL	Added draft input chapter 1,2, and 3.5
v1.3	2025-06-23	Rastislav Toman/CVUT, Felix Tischer/VIF	Added input chapter 3.1, 3.2, and 3.4
v1.4	2025-06-24	Nicola Contartese/VIF	Review and final edits
v1.5	2025-06-30	Tobias Lorscheider/VIF, Rastislav Toman/CVUT, Dionysios Panagiotopoulos/ KUL	Implementation of reviewer's comments
v1.6	2025-06-30	Nicola Contartese/VIF	Formal review and release

Documentation of Delayed Submission

Planned Date	M15 | 2025-03-31
Actual Date	M18 | 2025-06-30
Reasons causing delay	Available CAD models of the demo vehicles needed to be adapted to the required level of detail for proper NVH modeling.
Effects on follow-up activities and other WPs/tasks	There is no impact on the overall project timeline.
Mitigation measures	Closer communication between partner involved and OEMs.

Table of Contents

List of Figures

List of Tables

1. Executive Summary

Deliverable D4.2 outlines the development of individual models to assess the thermal, electrical and mechanical behavior of the GIANTS examined vehicles. Additionally, it outlines the development of the simulation platform where models can be integrated in a modular way. It incorporates input from original equipment manufacturers (OEMs), component suppliers, and user/stakeholder needs gathered in the previous work package 2. The present document explains mainly the methodology used within these models and the key findings of the respective analyses in terms of battery electric and thermal performance, together with the NVH characteristics of such vehicles. Finally, it investigates the potential influence of electrical, thermal, and mechanical effects on the Remaining Useful Lifetime.

Objectives

The aim of Task 4.2 was to develop an integrated, real-time capable simulation environment for adaptive energy management and end-of-life (EOL) prediction of key vehicle components. In line with the GIANTS project's objectives, this task focused on the modular integration of electrical, thermal, and mechanical models of vehicle subsystems, enabling comprehensive system-level simulations. The deliverable also targeted the development of low-cost degradation models to estimate battery lifetime and performance over repeated charge-discharge cycles, while ensuring predictive capabilities for thermal safety and noise-vibration-harshness (NVH) performance. A special emphasis was placed on enabling co-simulation with proprietary models via black-box interfacing to preserve intellectual property while supporting full system evaluation.

Progress Achieved

Deliverable D4.2 presents the GIANTS co-simulation platform built using Model. Connect, successfully integrating component models such as the battery modules (electrical and thermal), charging station, powertrain, solar panel, vehicle dynamics, and Vehicle Control Unit (VCU). A physics-based 1D thermal model for the battery was implemented in Matlab Simscape and evaluated across nine driving scenarios, including WLTC, WMTC, and MIDC cycles. A similar thermal model for the charging station was developed, supporting dynamic cycling studies by thermally switching between charging and driving states. Battery aging was modelled using low-cost formulations capturing capacity fade, resistance growth, and calendar aging. Furthermore, NVH performance was evaluated using Finite Element Methods, focusing on the acoustic field at the driver's ear and the vibrational transfer path effect on potentially critical components. Finally, estimation of remaining lifetime was performed using degradation and fatigue models regarding the battery and vibrational loading, respectively. Finally, this proposed simulation platform advances the state-of-the-art by enabling predictive, cross-domain simulation of thermal, mechanical, and aging effects in frugal electric vehicles, while maintaining scalability and industrial relevance.

Keywords: Co-simulation, Thermal Modelling, Battery Lifetime, NVH, Real-Time Simulation, Frugal Electric Vehicles

2. Objectives

In this chapter the objectives of deliverable D4.2 are being described. In addition, the work performed in the tasks T4.2 is being summarized and linked to the overall GIANTS mission.

The GIANTS platform is being developed among different OEMs, component suppliers and research partners. According to the GIANTS Grant Agreement the work package WP4 consists, among others, of the following main objectives:

- To develop a modular, real-time capable co-simulation platform that integrates multi-physics domains (electrical, thermal, mechanical), enabling system-level analysis and virtual prototyping of frugal electric vehicles.
- To implement realistic electrical models of battery modules and powertrain components (including inverter and motor) for integration into the overall simulation framework.
- To develop a physical thermal simulation model for vehicle battery modules and the charging station, assessing component temperature behavior under dynamic use conditions.
- To implement models for estimating battery lifetime based on thermal cycling, SOC usage, and calendar aging factors.
- To assess the internal acoustic comfort and vibration levels of the driver cabin using finite element simulations and identify critical NVH transmission paths.
- To evaluate the long-term structural and acoustic integrity of vehicle components under vibration-induced fatigue, complementing thermal degradation models.

According to the above objectives, the main achievements included in D4.2 are described below:

- Established a **co-simulation platform** using Model. Connect, integrating GT-Suite models, Matlab/Simulink models, and compiled FMUs.
- Successfully simulated full vehicle behavior across **driving, charging, and cycling scenarios**, including environmental variability.
- Ensured **modularity and IP protection**, enabling model updates or replacements without system reconfiguration.
- Demonstrated **centralized scenario control**, allowing users to adjust parameters and evaluate system response in different configurations (vehicle variants, track types, temperatures).
- Implemented **battery electrical models** (in GT-Suite and Simulink) considering real-world load profiles and charge/discharge dynamics.
- Linked electrical models to **thermal outputs (heat losses)**, enabling integrated thermal evaluation.
- Modelled **powertrain components** (inverter, motor, reducer) and integrated them into driving cycle simulations.

- Created a **1D thermal model in Matlab Simscape** based on heat generation and transfer equations.
- Simulated **9 thermal scenarios** with varying driving cycles (WLTC, WMTC and MIDC) for different vehicles and battery configurations.
- Developed a concept of a **modular thermal model** of the charging station supporting simultaneous battery charging with thermal feedback.
- Introduced **thermal switches** for co-simulation, enabling dynamic coupling between the vehicle and charging station.
- Achieved **co-simulation-ready thermal models** with defined I/O ports, supporting integration into the larger system.
- Implemented **capacity fade and resistance growth models** using low-cost, analytical formulations.
- Executed **cycling studies with repeated charge/discharge sequences**, monitoring thermal response and estimating degradation.
- Developed framework to simulate **calendar aging** effects as a function of time, SOC, and temperature.
- Built **FEM-based acoustic and structural vibration models** of the TUX Mobility vehicle cabin.
- Focused analysis on **driver's ear zone**, ensuring practical relevance for perceived comfort.
- Applied **high-order FEM** techniques to capture acoustic response in the 20–1000 Hz range with improved computational efficiency.
- Simulated **acoustic wave propagation and structure-borne noise** to identify key transmission paths and resonances.
- Identified **NVH-critical zones** using FEM, which can inform material choice and design for fatigue-sensitive regions.
- Supported future strategies for **optimizing lightweight acoustic treatments** under frugal vehicle constraints (cost, weight, manufacturability).

In total, the objectives of WP4 have been achieved among the different GIANTS partners. The results included in D4.2 and the work performed in Tasks 4.1 and 4.2 pave the way for the successful implementation of Tasks 4.3 and 4.4 and aiming at the development of efficient digital twins.

3. Description of Work

This chapter provides a comprehensive overview of the core components and methodologies utilized throughout the course of Task 4.2. It outlines the simulation infrastructure and modelling strategies used to evaluate the systems performance from multiple perspectives, including the electrical and thermal model, as well as NVH and lifetime assessment. Each of these aspects of the modelling and simulation process, that are contributing to an integrated approach for system evaluation and optimization, are described in the following subchapters.

3.1 Simulation platform

3.1.1 Introduction to the platform

The aim of the GIANTS co-simulation platform is to enable the cooperative development of lightweight electric vehicle platform equipped with swappable battery modules and a solar roof panel. As all these components involve different contributors, software, and physical domains (software, mechanical, electrical, thermal), the co-simulation platform integrates all these components into a single simulation system that allows all project participants to carry out simulations and/or optimize to the system.

The platform allows changing parameters at a central point and relaying these changes to the components, such that one can simulate the different vehicles being developed under different scenarios and environments. Models of the same component can also be easily swapped out with each other to study the influence of different layouts or levels of fidelity.

Current iteration of the GIANTS co-simulation platform uses Model. Connect software for the co-simulation integration. Specific sub-models are built with GT-Suite and Matlab/Simulink.

3.1.2 Introduction of co-simulation components

The co-simulation, as well as the vehicles themselves, consists of multiple subsystems and components. The main sub-systems are shown in Figure 3-1. Within the co-simulation platform, these are not necessarily congruent with real physical components, e.g. the battery module is split into two simulation models, one containing the electrical part, and the other containing the thermal part. The main features of each sub-system in Figure 3-1, together with the relevant data, are described in this chapter; details on the physics of these sub-models, together with example studies, are then in the following chapters.

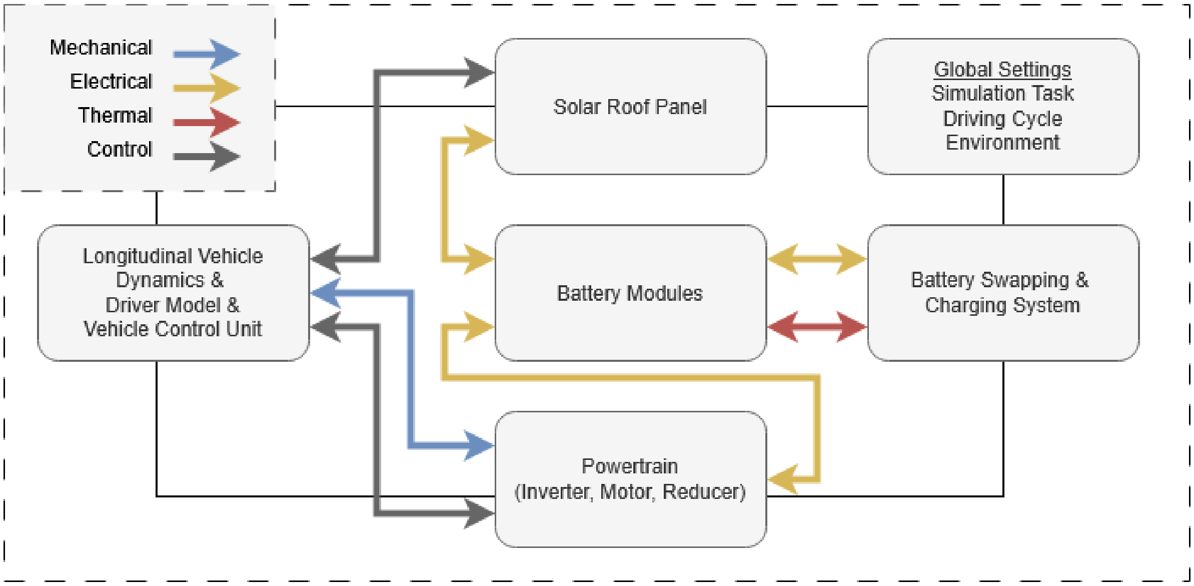

Figure 3-1: Co-simulation components and their connections.

Longitudinal vehicle dynamics and driver model

This sub-system, built with GT-Suite, contains the 1D longitudinal model based on vehicle resistances. This sub-system also contains the driver model, together with simplified VCU and BMS models.

Table 3-1 sums-up the characteristics of three selected vehicles variants that are used in example studies in the following chapters. CM2 is L5e-B cargo vehicle for the advanced market, TX1 a passenger L5e vehicle for emerging market, and finally the SQ1 is a passenger L6e vehicle.

Table 3-1: Input Characteristics of the GIANTS Demonstration Vehicles

Vehicle characteristics	CM2	TX1	SQ1	Unit
Vehicle total mass	500	450	380	[kg]
Passenger mass	75	75	75	[kg]
Vehicle drag coefficient	0.60	0.65	0.487	[-]
Vehicle frontal area	1.90	2.12	1.4	[m^2]
Tire rolling resistance factor	0.008	0.008	0.015	[-]
Tire rolling radius	0.253	0.253	0.253	[m]

Powertrain (including the E-motor, inverter, and gearbox)

The entire powertrain including the E-motor, inverter, and gearbox is modelled also in GT-Suite – here with only one technical option of powertrain from Valeo. Table 3-2 sums-up its main parameters. The last parameter (not present in Table 3-2) represents the on-board power consumption which includes heating, or air-conditioning, and is therefore variable based on use case.

Table 3-2: Input characteristics of the GIANTS powertrain

Powertrain characteristics	SMMG	
E-Motor maximum power	8.0	[kW]
E-Motor maximum torque	35	[Nm]
E-Motor maximum speed	11 000	[RPM]
E-Motor maximum efficiency	94	[%]
Final drive gear ratio	16.01:1	[-]
Final drive efficiency	97	[%]

Battery modules

As it was already mentioned, the battery modules are simulated within two separate sub-systems:

- Electrical and aging phenomena in GT-Suite.
- Thermal behaviour in Matlab Simscape.

A base building block of our battery systems is the LG M50T Li-ion 21700 NMC cell. There are three main battery module configurations for our following studies: 13s10p (13 cells in series, 10 in parallel), 14s10p, and 14s9p. Table 3-3 gives the parameters of these different configurations: modules with 14 cells in series operate at higher system voltages, which is generally beneficial for overall system efficiency.

Table 3-3: Input characteristics of the battery modules

Battery module characteristics	13s10p	14s10p	14s9p	Unit
Nominal voltage	47.5	51.1	51.1	[V]
Maximum voltage	54.6	58.8	58.8	[V]
Nominal power	2.37	2.56	2.56	[kW]
Peak power	5.69	6.13	6.13	[kW]
Nominal capacity	2.07	2.26	2.00	[kWh]
Peak capacity	2.37	2.55	2.30	[kWh]

Battery charging and swapping system

An important feature of GIANTS vehicle platform is represented by the swappable battery modules. These can be charged externally, and individually from one another. This sub-system handles the charging simulations of the separate battery modules, including the thermal behaviour.

Solar roof panel

The solar roof panel provides power for charging the batteries on-board, depending on the location and time of day. It consists of a pre-calculated lookup-table integrated into Matlab. The solar roof panel's power output is dependent on the location and datetime – which is why these two parameters are needed for the co-simulation. There are four locations for which data is available, and that represent places with little, medium, and high solar irradiation in the EU: Madrid, Bern, Amsterdam, and Stockholm.

Global Simulation Settings

Considering the input needed for the several subsystems presented above, several global co-simulation parameters can be set to vary the vehicle configuration and environment, as shown in Table 3-4 (showing some possible example settings). These parameters can be varied case-by-case to study the different influences.

Table 3-4: list of global co-simulation parameters

Parameters	Possible value examples
Vehicle	TX1, SQ1, CM2
Driving Cycle	WLTC, WMTC, MIDC, CLTC-C
Ambient Temperature	-10°C, 20°C, 40°C
Location	Madrid, Amsterdam
Date and Time of Day	2025-02-25T15:30:00
Battery module configuration	13s10p, 14s9p, 14s10p
Number of battery modules	4, 10, 12

3.1.3 Simulation Tasks

Three main types of simulation are considered in this study, each fulfilling a specific goal.

Vehicle Driving Cycle Simulation

This first simulation type aims to evaluate the energy consumption and to estimate the electrical range for the different driving conditions. Within our studies, we are using 6 different standard or non-standard vehicle driving cycles suitable for L-class vehicles. Figure 3-2 shows the velocity profiles, while Table 3-5 gives an overview of all cycles.

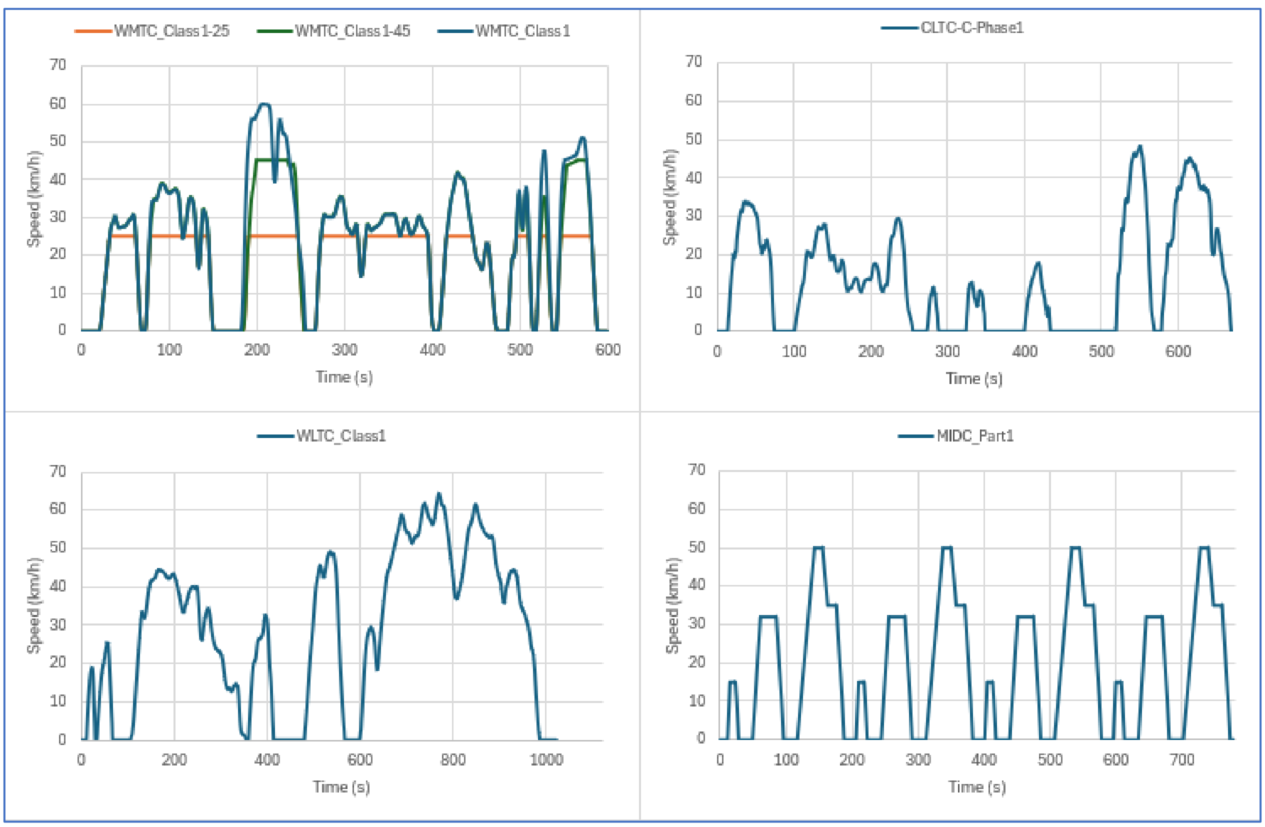

Figure 3-2: Overview of the used driving cycles

Table 3-5: Overview of the driving cycle characteristics

Drive Cycle	CLTC-C Phase1	WMTC Class1	WMTC Class1-45	WMTC Class1-25	WLTC Class1	MIDC Part1	
Duration	669	600	600	600	1022	780	[s]
Distance	2.45	4.07	7.6	5.88	8.09	3.99	[km]
Avg. speed (incl. stops)	13.17	24.44	22.78	17.63	28.50	18.44	[km/h]
Avg. speed (excl. stops)	20.82	29.81	28.09	21.74	35.35	27.24	[km/h]
Max. speed	48.1	60.0	45.0	25.0	64.4	50.0	[km/h]
Avg. acceleration	0.42	0.72	0.64	0.77	0.33	0.64	[m/s^2]
Max. acceleration	1.47	2.50	1.60	1.60	0.81	1.04	[m/s^2]
Avg. deceleration	-0.45	0.71	-0.69	-0.80	0.39	0.75	[m/s^2]
Max. deceleration	-1.42	-2.00	-1.85	-1.72	-1.14	-0.93	[m/s^2]
Acceleration	22.72	26.88	26.33	13.33	21.43	21.54	[%]
Deceleration	21.52	27.21	24.33	12.67	18.00	18.46	[%]
Cruise	19.01	29.05	30.43	55.09	41.68	29.23	[%]
Idle	36.74	17.03	18.9	18.9	18.98	30.90	[%]

It must be noted that WMTC Class1-25 and WMTC Class1-45 are simple variations of the WMTC Class1 cycle, with maximum vehicle speed capped at 25 or 45 km/h respectively. In addition to these drive cycles, vehicle acceleration simulations fall also within this type of simulation.

Charging Process Simulation

The second simulation type consists of charging process simulations. These simulations involve the Battery charging and swapping sub-system, together with Battery modules sub-system, but without the vehicle related sub-systems. Here, the goal is usually to study the charging speed, and temperature evolution of battery modules during charging event.

Cycling Study Simulation

The last simulation type is a combination of both abovementioned simulation types. It involves a repetition of charging and discharging event of the battery to assess the cell aging, or temperature evolution.

3.2 Simulation platform – vehicle and electrical modelling

This chapter describes two main parts of the simulation platform: longitudinal vehicle model, and electrochemical battery model.

3.2.1 Vehicle longitudinal dynamics and powertrain model

For the vehicle's dynamic driving events evaluation, a GT-Suite longitudinal vehicle dynamics model (1D model based on vehicle resistances) was built, with map-based powertrain component's efficiencies (E-motor, gearbox etc.). It contains a driver model that follows a prescribed vehicle driving cycle, together with simplified VCU and BMS (Battery Management System), while 1D approach considers the vehicle mass and rotational inertias, aerodynamic drag, rolling resistance, and climbing resistance on slopes. VCU and BMS models mainly control that the battery and E-motor limits (electrical power, current, and voltage) are not violated in any powertrain mode (acceleration, recuperation braking, etc.).

The powertrain architecture of 3-wheeler or 4-wheeler L-category vehicles consists generally of an E-motor connected to the driven wheels via a reduction gearbox with a constant gear ratio. The E-motor is represented by a map-based model, with efficiency and performance characteristics defined as functions of E-motor speed (RPM), torque, and supply voltage (although in the following studies we only use one nominal voltage level). The E-motor efficiency map contains combined efficiency of the E-motor and power electronics. Gearbox efficiency is modelled in a similar way, as a map dependent on RPM and input torque. Both efficiency maps are also dependent on component's temperature, however this is not considered now.

3.2.2 Electro-chemical battery model

In order to simulate the different degradation and aging mechanisms of the battery cells, which are necessary to simulate the LCA (life cycle assessment) of the whole battery module, we are using a "Pseudo-2D" Doyle-Fuller-Newman (P2D) model [1], within the GT-AutoLion, that is also part of GT-Suite package. The model captures the electro-chemical reactions occurring inside a Li-ion cell and predicts the terminal voltage, current, power, heat rejection, and amount of lithium throughout the cell, simplifying the battery cell into three regions: cathode, anode, and separator with further spatial discretization. The GT-AutoLion battery model also considers the thermal evolution of the cell and different degradation mechanisms, such as film growth or active material losses [2]. User of the GT-AutoLion electro-chemical model has then the option to run the simulation with either "fresh" cells or "aged" cells. These degradation mechanisms, when calibrated, consider the thermal aging effect, together with calendar and cycle aging effects. Results in the example study of chapter 3.4.2 with LCA of a battery module.

Parameters, and different GT-AutoLion sub-models for LG M50T Li-ion cell that is a basis of our battery modules were calibrated and validated against the extensive measurements, considering SOC and temperature dependencies. Detailed process with OCV, and dynamic calibration, followed by calendar and cycle aging calibrations is outlined also in [2].

3.2.3 Example study of acceleration dynamics and vehicle energy consumption

The example study that is presented for this subchapter 3.2 is consists of two comparisons:

- The first comparison shows the vehicle acceleration dynamics, by evaluating the 0-45 km/h acceleration time.
- The second comparison shows energy consumption together with electrical range evaluation.

The goal in this example study is also to show and evaluate one of the possible "extreme" cases that all vehicles have only one battery module available. Both comparisons are for three GIANTS vehicles – CM2, TX1, and SQ1 (see Table 3-1), in combination with three possible battery modules from Table 3-3.

3.2.3.1 Acceleration dynamics

The first study compares the three GIANTS vehicles in 0-45 km/h acceleration test, as shown in Figure 3-3, with the aim to highlight the limiting component (E-motor or battery module) for different possible maximum C-rate levels (i.e., the charge or discharge rate of a battery relative to its capacity).

The best acceleration performance is achieved by the SQ1 vehicle, which is the lightest of the three concepts. All three vehicles are limited by the battery performance at lower C-rate; therefore, we see a difference for the 3 modules' configurations (14s10p offers the highest power, 14s9p the lowest). At C-rate of 4, the acceleration performance is limited by the E-motor performance.

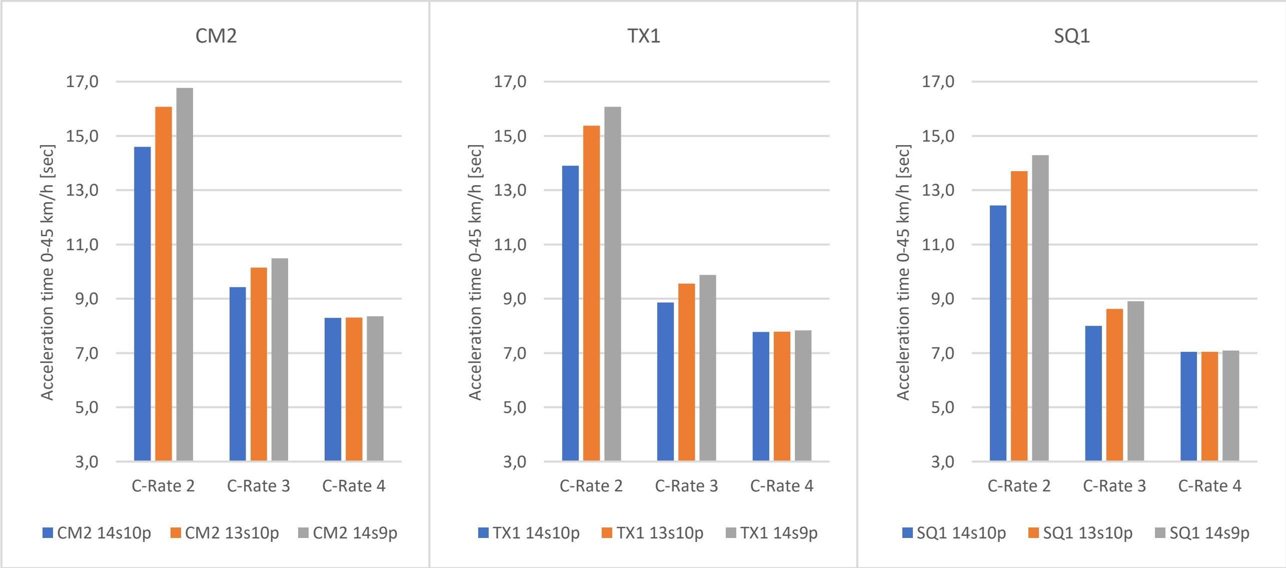

Figure 3-3: Acceleration dynamics results

3.2.3.2 Energy consumption and electrical range

In the second comparison of this study, the three selected GIANTS vehicles are compared in two different vehicle driving cycles: WLTC Class 1 and MIDC Part 1, using vehicle parameters from Table 3-1. A result of this study is the energy consumption for each vehicle with the different battery module configurations (again, using 1 module only), together with electrical range estimation: Figure 3-4 is for WLTC Class 1 and Figure 3-5 for MIDC Part 1.

Highest energy consumptions are achieved by the vehicle with the highest resistances in both vehicle driving cycles, which in this case is the TX1; the best performing vehicle is the SQ1. A very small difference in energy consumption between the three battery module configurations can be noticed because:

- there is no difference in vehicle mass, although the modules would have different mass;
- E-motor map used in the study is only for one voltage level, which nullifies the advantage of higher-voltage systems for 14s10p and 14s9p compared to 13s10p;
- during a single repetition of a vehicle driving cycle, the SOC change is also not enough to affect the battery efficiency more.

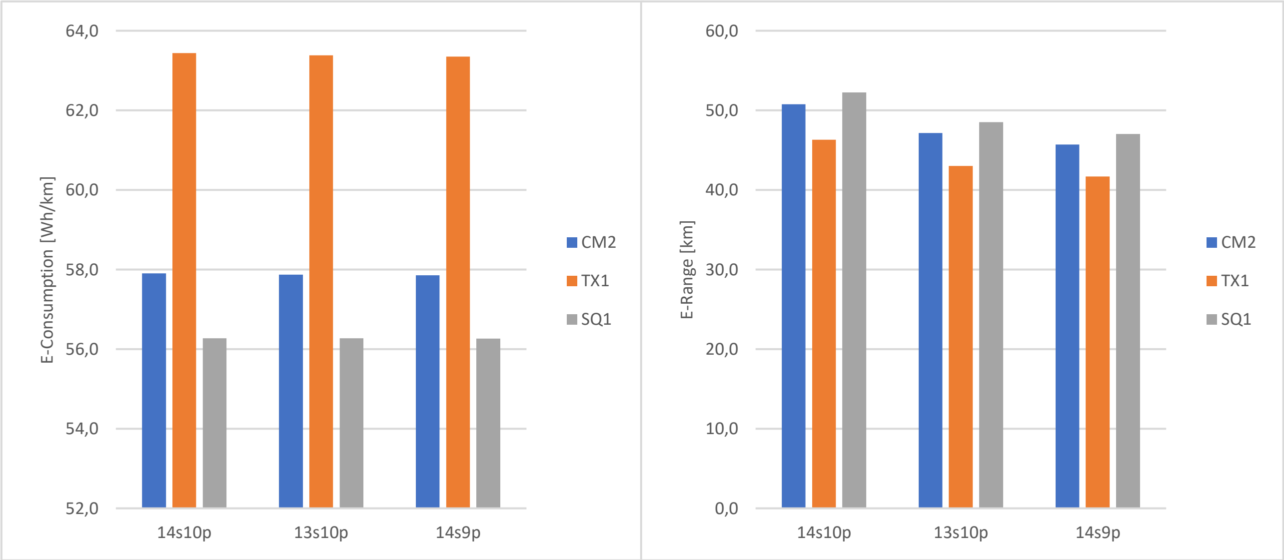

Figure 3-4: WLTC Class 1 energy consumption and electrical range evaluation

Looking onto the right-side column diagrams of Figure 3-4 and Figure 3-5 we can see a difference in estimated electrical range for “1-module” driving. Here, the highest ranges are achieved in both vehicle driving cycles for the best energy consumption vehicle SQ1 in combination with 14s10p module, that has the highest capacity. Generally, higher the module’s capacity, higher the electrical range.

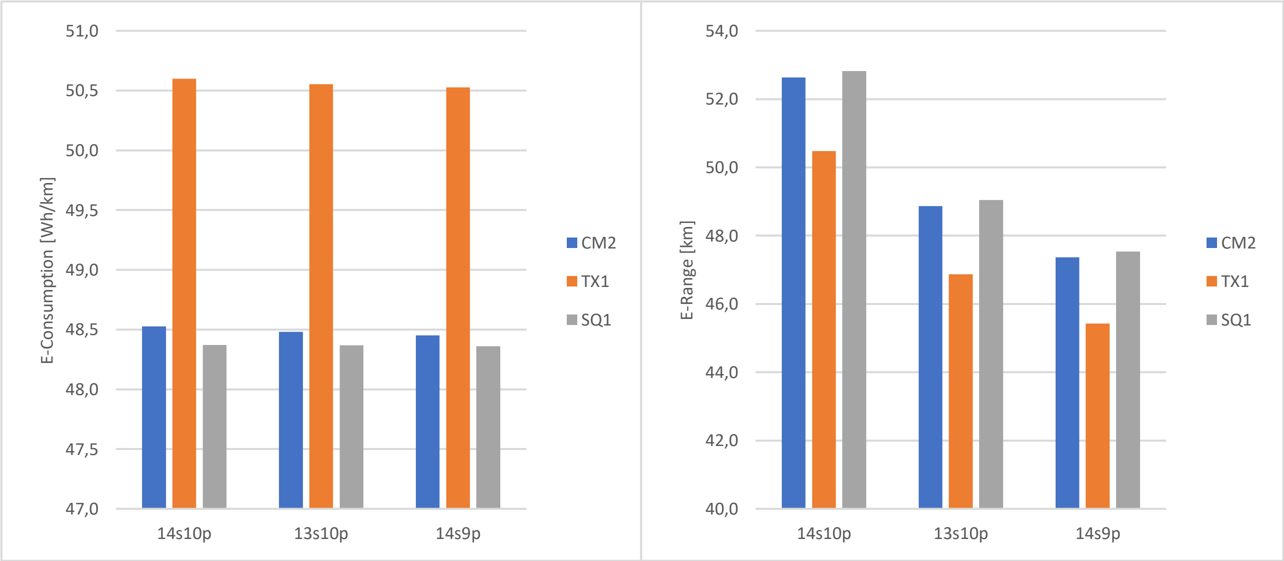

Figure 3-5: MIDC part 1 energy consumption and electrical range evaluation

3.3 Simulation platform – thermal modelling

This section focuses on the implementation of the thermal model required for the simulation platform. Fundamental principles, mathematical framework and computational techniques are described.

A brief overview of the most important equations that the model is based on are given. Afterwards, the implementation to the simulation environment is shown, and different scenarios to test the system are explored, emphasizing the assumptions and boundary conditions relevant to the practical application.

3.3.1 Aim of the thermal assessment platform

The aim of the thermal simulation platform is to provide a virtual testing environment that allows you to model, analyze and optimize thermal behavior of the designated components of a vehicle under various operating conditions, without the need for physical prototyping and testing. Since temperature is one of the most critical factors affecting performance, safety and lifespan of a battery, it is crucial to have a good understanding of the requirements, as well as the behavior of the system in the early development phase [3]. Therefore, the primary objectives of such thermal assessment are predicting thermal performance, design, and optimizing the thermal management system. This is to ensure the safety, reliability, efficiency, and performance of each component.

3.3.2 Theoretical background

Battery thermal modeling is crucial for maintaining optimal performance, ensuring safety, and preventing damage from overheating. The latter can lead to degradation in performance and thus a reduced lifespan. Several factors affect the thermal behavior of a battery, such as heat generation, heat transfer throughout the cells, as well as the cell design itself [4]. Such thermal model can have different levels of complexity, one-, two- and three-dimensional, where the one-dimensional model consists of a simplified cell design and operating conditions, while the three-dimensional model provides temperature gradients throughout the cell. In Tasks 4.1 and 4.2 of the GIANTS project, a one-dimensional simulation is set up due to its low-cost modelling and low simulation power requirements while still providing the necessary outputs.

The 1D simulation model describes the temperature change as the sum of generated heat in the system and dissipated heat that leaves the system. This is defined by the following basic heat balance equation:

$$Q_{acc} = Q_{gen} - Q_{diss}$$

Three losses are considered: first, due to the current I flowing over the internal resistance R_i, second, the heat due to the chemical reaction in the cell during charging and discharging and third, the entropy change where I is the current flowing through the battery, T the temperature and dE/dT the entropy heat coefficient [5]:

$$Q_{ohmic} = I^2 \cdot R_i$$

$$Q_{reaction} = I \cdot (V - OCV)$$

$$Q_{entropy} = I \cdot T \cdot \frac{dE}{dT}$$

The sum results in the heat generated in the battery cell are according to the following equation:

$$Q_{gen} = I^2 \cdot R_i + I \cdot T \cdot \frac{dE}{dT} + I \cdot (V - U)$$

The heat loss to the environment can be described by three different heat transfer processes: conduction, convection, and radiation. The main heat transfer processes modelled in the 1D simulation are the conduction through the thermal masses defined as following, where k is the heat transfer coefficient, A the area and D the thickness of the object, T_A and T_B are the two temperature regions:

$$Q = k \cdot \frac{A}{D} \cdot (T_A - T_B)$$

The convective heat transfer is modelled as following, where also k is the heat transfer coefficient, A the area and of the object, T_A and T_B are the two temperature regions:

$$Q = k \cdot A \cdot (T_A - T_B)$$

The radiative heat transfer is neglected.

The battery temperature changes in the cell due to the heat accumulation can be described as the following, where M_{th} is the thermal mass of the battery and dT/dt is the temperature change rate:

$$Q_{acc} = M_{th} \cdot \frac{dT}{dt}$$

This leads to the overall heat balance equation of the model and is defined as:

$$M_{th} \frac{dT}{dt} = I^2 \cdot R_i + I \cdot T \cdot \frac{dE}{dT} + I \cdot (V - U) - k \cdot A \cdot (T_A - T_B)$$

Batteries are significantly temperature dependent, i.e. cold temperatures have an impact on two major factors: firstly, the chemical reaction is slowed down, and secondly, the internal resistance is increased causing a higher voltage drop. As a result, the capacity is also reduced in cold weather. On the other hand, in hot climates, the chemical reaction is accelerated, leading to faster discharge rates, reduced capacity, and therefore increased degradation [6].

3.3.3 Thermal model of the battery for vehicle

In the following sections 3.3.3 and 3.3.4, the implementation of the thermal models of the battery and the charging station that are necessary to fulfill the described simulation tasks in section 3.1.3 are described. Beginning with the first simulation task, the following model of the battery is required for the thermal evaluation of transient behavior, e.g. during driving cycles, and sets the basis for the adapted models in section 3.3.4.

The developed battery thermal model is a physics-based 1D simulation model using Matlab Simscape. The heat generation and change in battery temperature is determined by the equations in section 3.3.2.

As shown in Figure 3-6, the thermal model consists of different thermal masses for the different structural components of the battery pack: aluminum cover plates, a conductive foam layer that connects cells and aluminum cover, plastic cell holder and PC/ABS edges. The battery cells are modeled as lumped thermal masses.

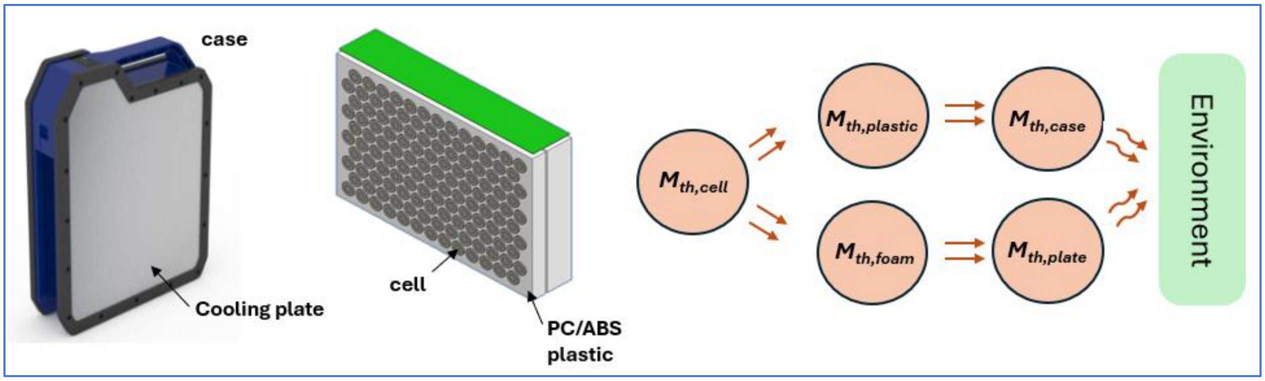

Figure 3-6: Thermal model schematic

The generated heat according to the mathematical models in section 3.3.2 is transferred via conduction through cell holder, the foam and the cooling plate, which is then released to the environment via natural convection. The following Table 3-6 shows the characteristics of the module, that are provided within the consortium and are based structural characteristics and measurements of the model.

Table 3-6: Overview of thermal characteristics of the module.

	Thermal mass [J/K]	Area [m²]	Thickness [m]	HTC conductive [W/(K*m)]	HTC convective [W/(K*m²)]
Battery	9360	-	-	-	-
Foam (side)	940	0.42	0.002	2.3	-
Cell holder(edge)	940	0.22	0.002	0.2	-
Plate (side)	1552	0.42	0.002	237	-
Case (edge)	1054	0.22	0.002	0.2	-
Environment	-	0.64	-	-	20

The implementation of the thermal model in Simscape can be seen in the following Figure 3-7. For development purposes a simple electric circuit is set up in which current profiles are fed to simulate battery loads and generate heat under different driving conditions, indicated by the blue color. The electric battery model also contains the thermal mass of the battery.

The thermal circuit, displayed in orange, contains the thermal masses of the cell holder, aluminum plates and casing, as well as the heat transfer components. Two temperature sensors observe the temperature of the battery as well as the cooling plate to give feedback to the overall simulation model.

The model does not contain any active or passive cooling through an air flow or coolant pipes but can be used to determine if additional cooling is necessary. The only heat sink in the model is natural convection to the ambient.

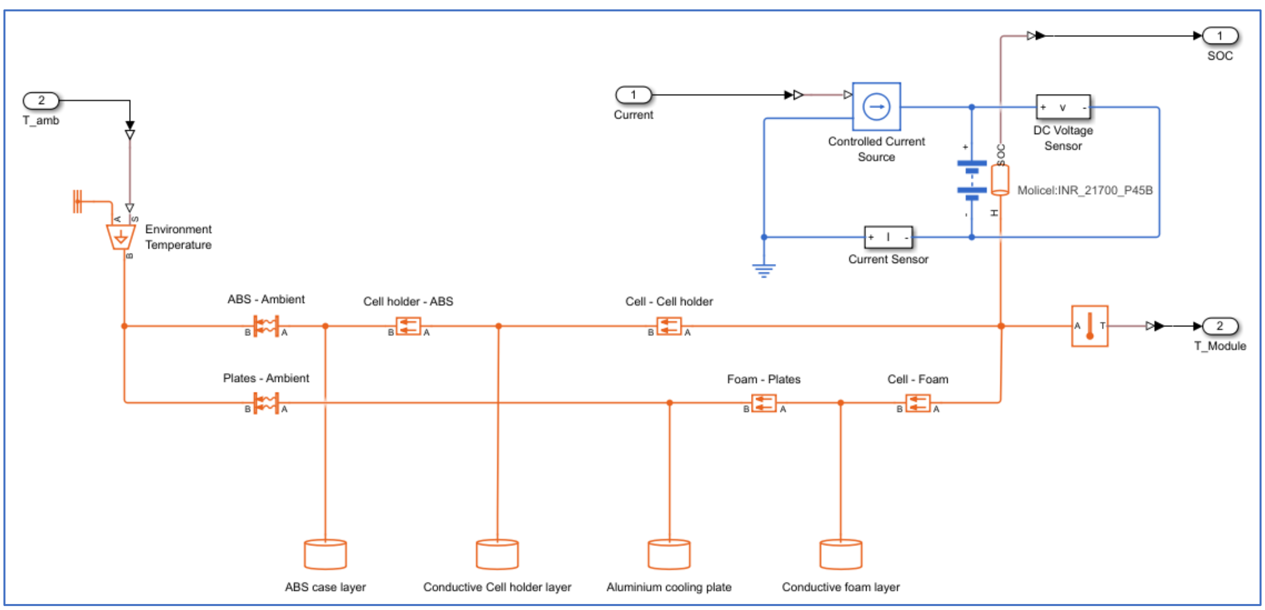

Figure 3-7: Thermal Simulation Model

In a next step, the thermal model is decoupled from the simple electric circuit and an external input port will be added to prepare the model for co-simulation. The model has in total two input and two output ports. The block shown in Figure 3-8 is used for co-simulation purposes.

Input: Battery heat losses (Q_Bat), ambient temperature (T_amb)

Output: Battery temperature (Bat_Temp_degC), temperature of cooling plate (Plate_Temp_degC)

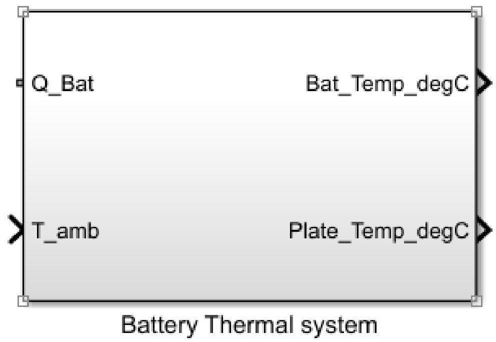

Figure 3-8: Thermal Model Block in Matlab Simulink

3.3.3.1 Example study: Battery thermal model in vehicle operation

For the evaluation of the thermal model, different simulation scenarios are defined according to the target market environment and requirements. In total three different vehicles (CM2, TX1 and SQ1), three driving cycles (WLTC, WMTC and MIDC) and three different battery configurations (14s10p,14s9p and 13s10p) are simulated at 40°C ambient temperature. More detailed vehicle and driving cycle data can be found in section 3.1.2. Based on these boundary conditions, different load profiles are applied to the battery thermal model. For each case, only one battery module at a starting SOC of 95% is used. The following Table 3-7 gives an overview of the nine conducted simulation cases at different conditions. For simulation 8 and 9 two worst case scenarios are generated. The TX1 vehicle is modified and set to 800kg vehicle weight and then operated at 40°C ambient temperature for the WMTC and 11x WMTC to deplete the battery entirely and observe thermal behavior.

Table 3-7: Overview of simulation cases for thermal evaluation of battery module.

<table>
<tr><th>ID
[-]</th><th>Driving Cycles
[-]</th><th>Vehicles
[-]</th><th>Battery configuration
[-]</th><th>Ambient temperature
[degC]</th></tr>
<tr><td>Sim#1</td><td>WLTC</td><td rowspan="3">CM2</td><td rowspan="5">14s10p</td><td rowspan="9">40</td></tr>
<tr><td>Sim#2</td><td>WMTC</td></tr>
<tr><td>Sim#3</td><td>MIDC</td></tr>
<tr><td>Sim#4</td><td rowspan="4">WLTC</td><td>TX1</td></tr>
<tr><td>Sim#5</td><td>SQ1</td></tr>
<tr><td>Sim#6</td><td rowspan="2">CM2</td><td>14s9p</td></tr>
<tr><td>Sim#7</td><td>13s10p</td></tr>
<tr><td>Sim#8</td><td>WMTC</td><td rowspan="2">TX1 modified</td><td rowspan="2">14s9p</td></tr>
<tr><td>Sim#9</td><td>11x WMTC</td></tr>
</table>

The results of the first three simulation cases are shown in the following Figure 3-9 a). It shows that the WMTC is the most demanding driving cycle due to higher C-rates than the WLTC and MIDC. This leads to a slightly higher temperature increase of the module in the WMTC case. Due to its low operating currents and a battery thermal mass of 9360J/K, the temperature only rises by 0.5-1.2K. Comparing the different vehicle types for a WLTC under the same ambient conditions in Figure 3-9 b) shows similar behavior, i.e. that the battery temperature only increases slightly. The comparison of the different battery configurations in Figure 3-9 c) shows that there is only a small difference of 0.2K between the different battery types.

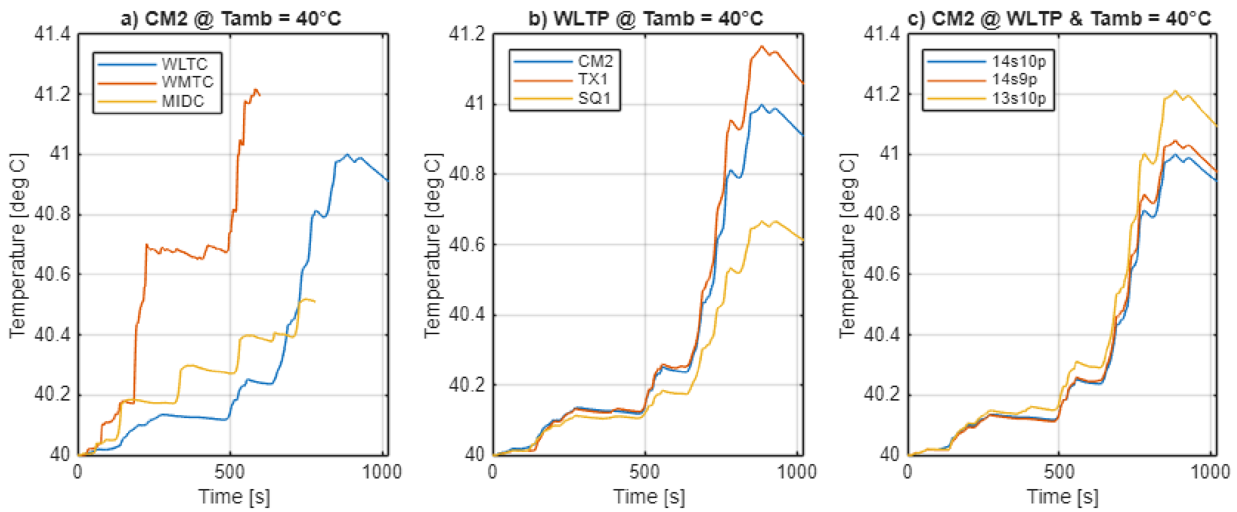

Figure 3-9: Simulation results battery temperature for simulation cases #1-7

Considering the results from simulation 1 to 7, a generic worst-case scenario is simulated as well (Case 8). The vehicle mass is set to the maximum vehicle weight of 800kg using the TX1 under the same ambient conditions for the WMTC driving cycle. Considering temperature and SOC dependency of the internal resistance, the battery losses reach a local maximum of around 420W at e.g. t=500s. Again, the temperature increase is low with around 2K, as shown in the following Figure 3-10 a).

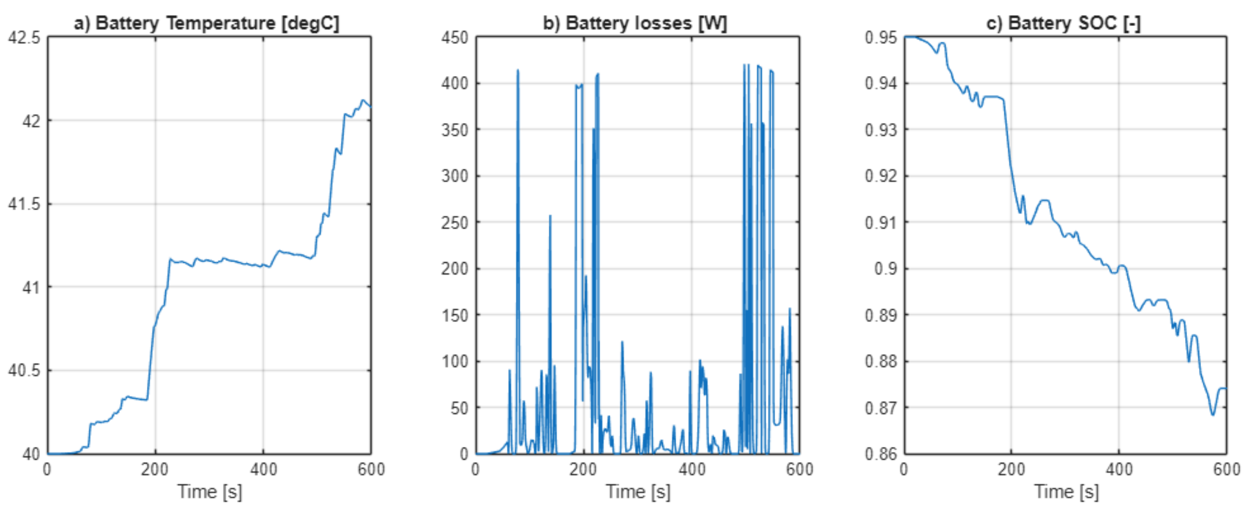

Figure 3-10: Example: Battery temperature increases for simulation case #8

Simulation case 9 is an extended version of case 8. The same model is simulated until the battery reaches 15% SOC, which results in 11 times the WMTC. The following Figure 3-11 shows that at the end of the simulation, the temperature increases faster due to higher losses, caused by the increasing internal resistance and increasing current due to low SOC.

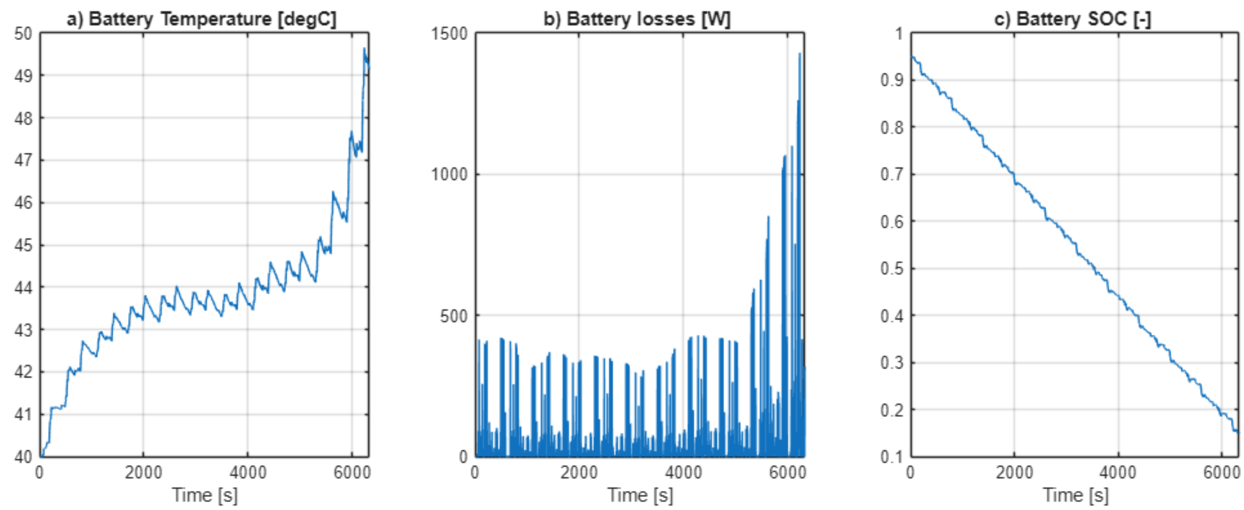

Figure 3-11: Example: Battery temperature increase for simulation case #9

Overall, the functionality of the battery thermal model in vehicle operation has been shown in this section. Simulating various driving cycle scenarios shows that the battery module remains within safe thermal limits (<45degC for Li-ion) for normal conditions (Case 1-7). Considering the generic worst case and depleting the battery fully in one run leads to a temperature increase of a round 9K during the most demanding driving cycle at a constant high ambient temperature of 40°C. At the current status of the model only natural convection is considered, a forced air flow due to the movement of the vehicle or a fan is neglected therefore the thermal behavior will improve by adding it. A simulation is not yet conducted for lower ambient temperatures but does not pose a problem considering the given results. However, the stated results are preliminary and work as a proof of concept for the proposed model implementation. In further evaluations also driving cycles with high demand such as driving up-hill at full load with low air flow are considered.

3.3.4 Thermal model of the battery for charging station

The different simulation tasks described in section 3.1.3 require certain capabilities from the thermal models. Due to the modularity of the batteries the model requires a thermal interface to the vehicle as well as to the charging station, which is also developed in the GIANTS project. Performing a cycling study, these interfaces switch during simulation between the vehicle and the charging station. The following Figure 3-12 illustrates the necessary interfaces. During vehicle operation, the sub models within the red dotted area are used, while during the charging process, the sub models within the green dotted area are used.

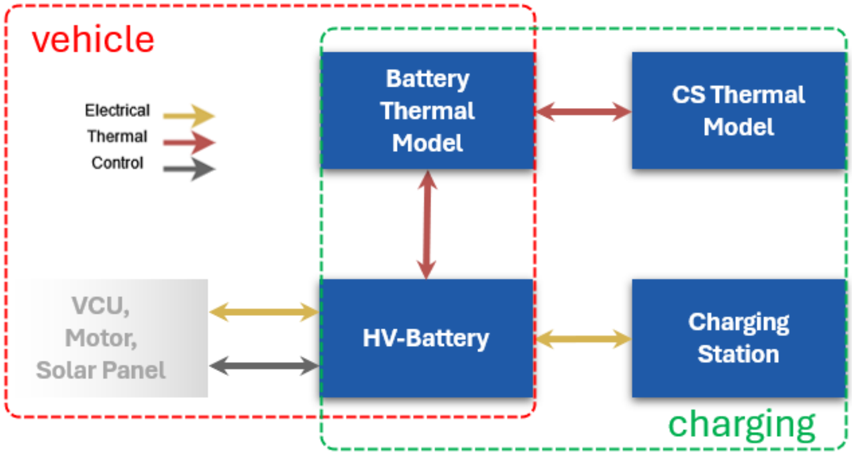

Figure 3-12: Interfaces during different operational processes.

To evaluate the battery during charging, a first simplified thermal model of the charging station is set up. Since the design is not final yet, a preliminary model has been implemented in Simscape. The current version of the model contains five modules for charging as well as the thermal model of the charging station. The following Figure 3-13 shows the top level of the charging station simulation model with the connected modules.

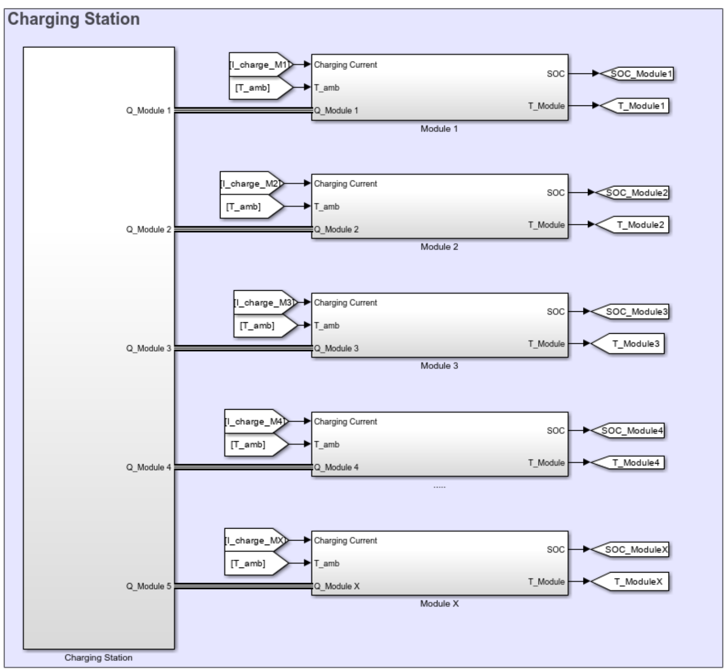

Figure 3-13: Charging station model top level

Five module slots are used independently for battery charging. As shown in Figure 3-14, the battery thermal model is similar to the model that is used for the vehicle simulation, but it requires certain adaptations for additional thermal connections to the charging station (marked in red).

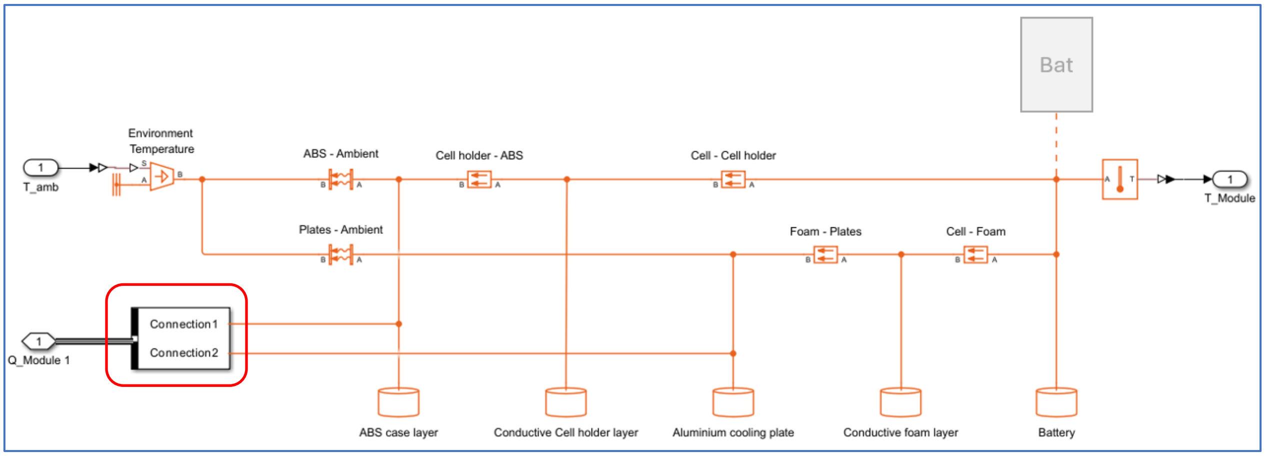

Figure 3-14: Adapted thermal model module with thermal connector to charging station

Since the design of the charging station is yet to be defined, a dummy model is used to simulate the thermal behavior of the charging station to demonstrate its functionality for battery swapping. On the right side of the following Figure 3-15, a concept of the charging station is shown, where the modules can be inserted into individual slots to be temperature conditioned via plates and an air-conditioned chamber. Each module is thermally connected to its individual thermal mass of the charging station. The thermal masses transfer heat conductively between each other and are connected to the environment via convective heat transfer.

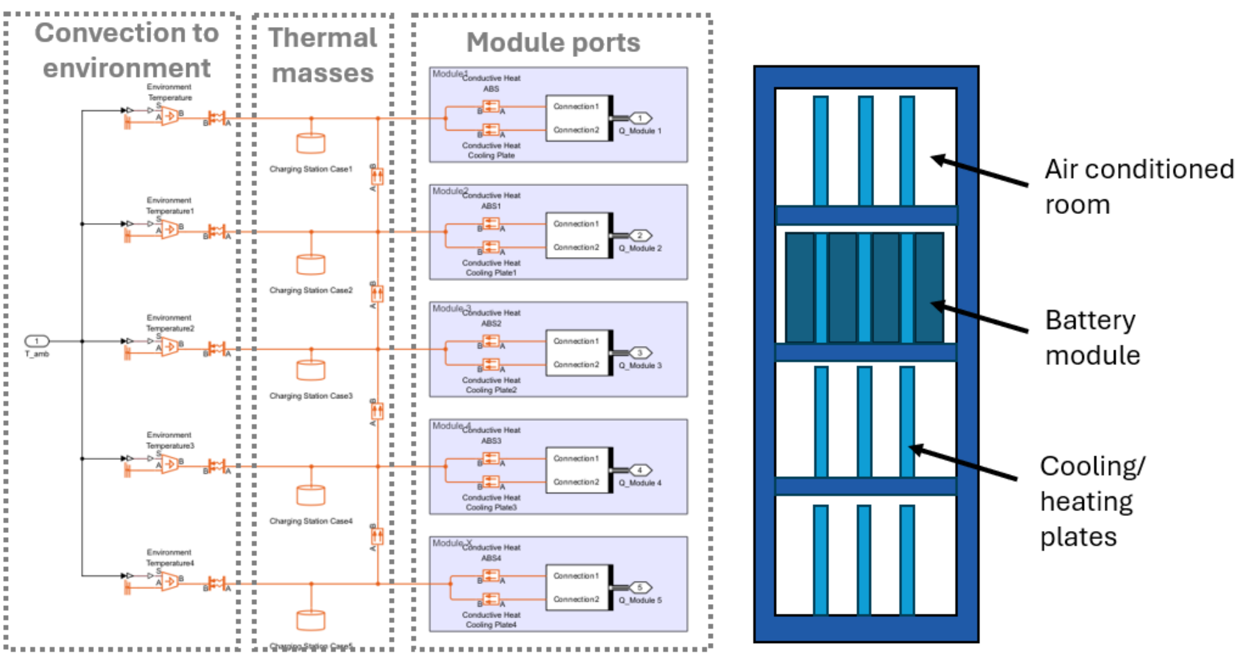

Figure 3-15: Thermal model concept of charging station

3.3.4.1 Example study: Battery thermal model in charging station operation

The second simulation task mentioned in section 3.1.3 describes the charging process of a battery module. The following results show the functionality of the thermal model for battery charging at 15% starting SOC 40°C ambient temperature. The charging current is set to 0.5C which results in a charging current of 25A, and the battery is decoupled when SOC of 95% is reached. The charging station is temperature conditioned to 25°C and cooling plates cool the battery during the charging process to around 23°C.

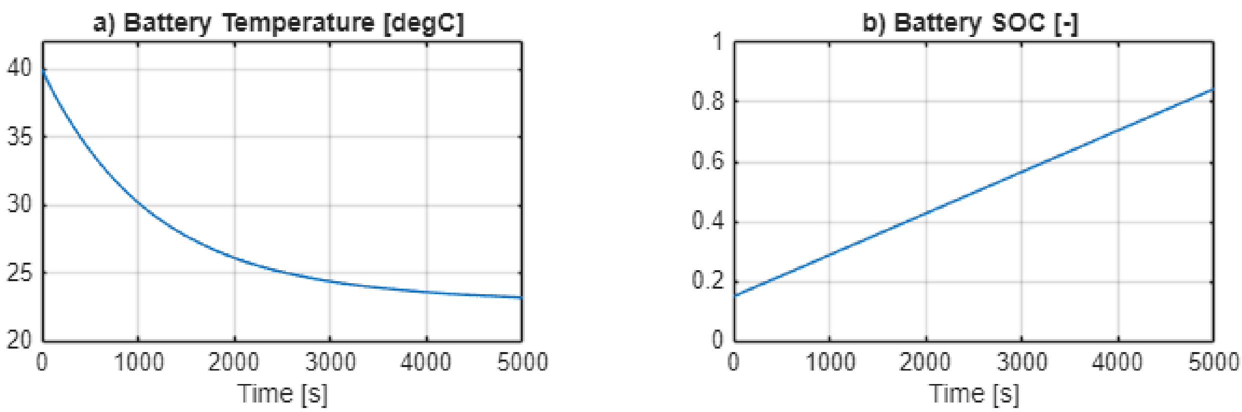

Figure 3-16: Example: Temperature during charging process

3.3.4.2 Example study: Battery thermal model cycling study

In the third simulation task, the model undergoes a cycling study where the battery repetitively switches between discharging during driving cycle operation and charging in the station. For that an additional thermal switch, marked in the red box, is added to the thermal model of the battery, that connects the battery thermal model to the charging station thermal model during the charging process and disconnects when the battery is connected to the vehicle.

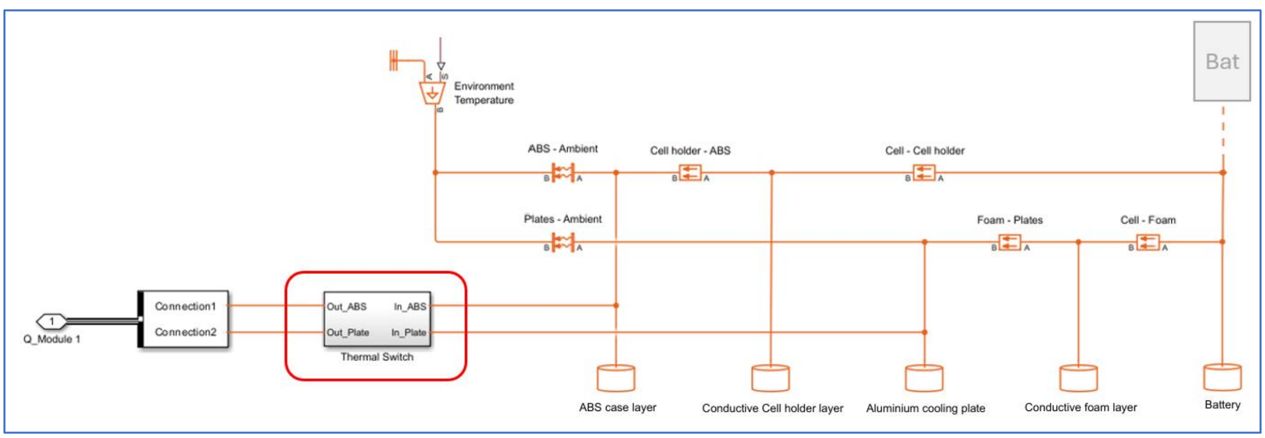

Figure 3-17: Battery thermal model with thermal switch

The model runs iteratively charging and discharging cycle. First the battery is connected to the charging station and charged to 95% SOC, then the model runs the WLTC until the battery is drained. The following Figure 3-18 shows 10 discharging/charging cycles. When the module is inserted to the charging station, it cools down to around 23°C, when operating it in the vehicle again, battery temperature rises to around 42°C during the whole driving cycle.

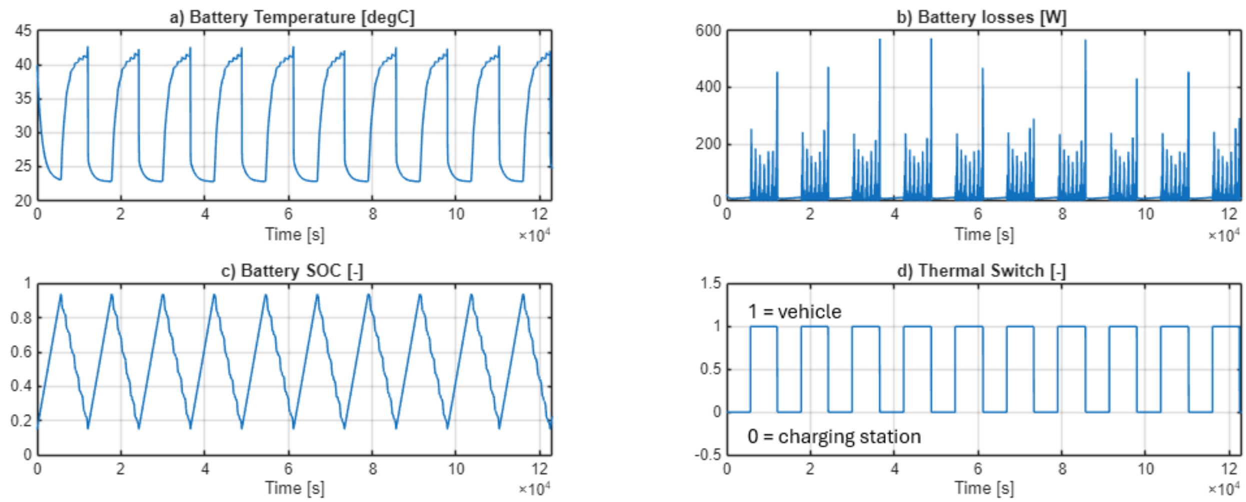

Figure 3-18: Proof of concept cycling study

The implementation and functionality of the battery thermal model and charging station thermal model for all three simulation tasks are described. All simulation models are based on provided data from the other WPs. However, for certain components such as the charging station, assumptions have been made due to the early stage of the development and must be adapted according to the final design of each component. The simulation results have yet to be validated as soon as the final models and the required measurement data are available. These results will be shared in the following deliverables.

3.4 Lifetime assessment

The lifetime of a battery is a critical parameter that determines its viability for long-term applications in electric vehicles. The following section gives a brief overview of different key mechanisms and their influence on the battery. Two example studies show the functionality and compare two different approaches with different level of complexity: a electro-chemical model using GT-AutoLion and a low-cost model based on simple mathematical equations.

3.4.1 Background

Several key components must be considered for battery lifetime assessment. The cycle life is defined by the number of complete charge and discharge cycles of the battery before its capacity drops below around 80% of its original capacity. Typically, lithium-ion batteries last for around 300 to 1000 cycles before reaching 80%. Influencing factors for the degradation are the depth of discharge, C-rates, temperature, SOC range and battery chemistry [7].

All these influencing factors refer to the terms of calendar and cycling aging, while calendar aging is a process that occurs also when the battery is not used, the cycling aging refers because of repeated charging and discharging of the battery. Modelling the degradation processes is a complex and cost-intensive task. The scope of this chapter is, however, to list and describe the effects of the heat on the battery lifetime. Then, GT-AutoLion electro-chemical model that is introduced in chapter 3.2.2, is also used within our simulation platform for the lifetime assessment studies of battery modules (chapter 3.4.2 shows an example study with GT-AutoLion models). Afterwards a simplified battery aging model is implemented based on analytical formulations and compared to the GT suite model. A more detailed modelling of the degradation process will come in the following deliverable, where the GIANTS Digital Twin will be presented.

Cycling aging

This term refers to the degradation of the performance and capacity of a battery over repeated charging and discharging cycles. It is one of the two major aging processes beside calendar aging. During charging and discharging a battery undergoes physical and chemical changes that gradually reduce the capacity. Different aging mechanisms take place as described in [8]. Main influencing factors of cycling aging are depth of discharge, C-rates, operating temperature and cell chemistry. This results in symptoms such as capacity fade, increased internal resistance, voltage changes and thermal issues, and overall efficiency decrease of the battery.

Calendar aging

Unlike cycle aging, calendar aging also takes place when battery remains unused, due to continuous chemical and physical processes in the cell. Understanding calendar aging is crucial for battery lifetime prediction, hence battery lifetime assessment in general [9] [10]. Calendar aging is strongly affected by the temperature, the state of charge and cell chemistry, therefore minimizing calendar aging involves storing the batteries at moderate temperatures and lower SOC levels. [11]

High Temperature influence on Aging

The two major aging factors, cycling and calendar aging, are significantly influenced by the operating and storage temperatures. High temperatures have a significant impact on the capacity fade and can increase sharply if operating over 40°C [8], especially for lithium-ion batteries. Key degradation mechanisms that are triggered by heat are SEI growth, electrolyte decomposition, cathode degradation and more. All these effects combined lead to a measurable rise in internal resistance, reduced power output and reduced efficiency. Experimental studies show that operating batteries at higher temperatures (30 to 45°C), can reduce cycle life by more than 50% compared to operation at 25°C [12]. To identify issues early and mitigate adverse behavior different strategies can be applied, such as the usage of lifetime prediction or predictive thermal management. Table 3-8 indicates some aging mechanisms in lithium-ion batteries that are related to heat and its effects.

Table 3-8: Battery aging mechanisms related to heat and high temperatures.

Mechanism	Description	Effect
Solid Electrolyte Interphase Growth [13]	The SEI layer on the anode thickens more rapidly at high temperatures, consuming lithium and increasing impedance.	Capacity fade and increased resistance
Electrolyte decomposition [14]	Elevated temperatures cause decomposition of the electrolyte solvents and salts.	Gas generation, pressure build-up, loss of ionic conductivity, and safety risks
Lithium plating [15]	At high temperatures combined with high charge rates or high SOC, localized overpotentials can cause lithium to deposit on the anode surface.	Short circuits and thermal runaway

Structural Degradation of Electrodes [16]	High temperatures induce phase transitions and particle cracking in cathode materials.	Permanent capacity loss

3.4.2 Example study: LCA of a battery module

The example study focuses on the LCA of a single 14s10p module, that is charged and discharged while driving the SQ1 L6e passenger vehicle during two consecutive years. This charge-discharge cycling focuses on single battery module, although in a vehicle while driving there are two modules. The study is focused on European-marked subjects and is assuming mild temperatures.

According to the GIANTS project partners' experience, the daily range for SQ1 vehicles can be from around 3 km/day up to almost 25 km/day. In this study we consider a daily drive of about 15 km/day, and 3 consecutive days without charging the battery modules. For 14s10p modules this represents about 50 % of battery SOC discharge. Then, each module will be charged separately. 80 such cycles are achievable during a year.

To summarize, one charge-discharge cycle of 14s10p in this study represents:

- First, discharging two battery modules while driving the vehicle 3-times about 15 km, using CLTC or WMTC Class1-45 vehicle driving cycles.
- Then, every 3 days charging the battery modules separately to 95 % SOC, by about 2 kW.
- We assume 80 cycles per year.

After running the battery modules' cycling, we test the vehicle performance with battery modules containing first the "fresh" cells and then "aged" cells after degradation. Both WMTC Class1-45 and CLTC cycles are used again for energy consumption and electrical range evaluation. For further comparison with WMTC Class1-45 and CLTC, we also added 600 seconds drive on constant vehicle speed of 45 km/h (noted Const45 in the following figures).

First, Figure *3*-19 shows the battery cell capacity loss during charge-discharge cycling. Both vehicle driving cycles lead to almost identical capacity degradation of about 2.6 %.

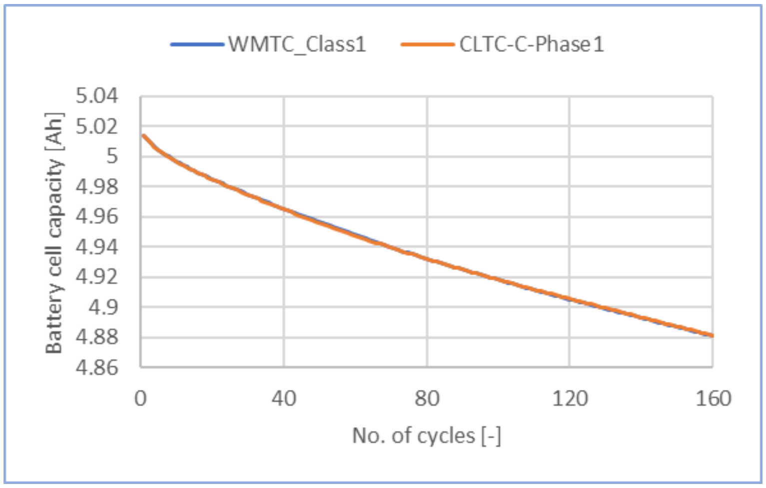

Figure 3-19: Battery cell capacity loss during 160 cycles

Figure *3*-20 – left, represents the energy consumption of SQ1 in these 3 different vehicle driving cycles. In each case, the energy consumption is higher for aged cells, with the highest difference of 2.5 % for WMTC.

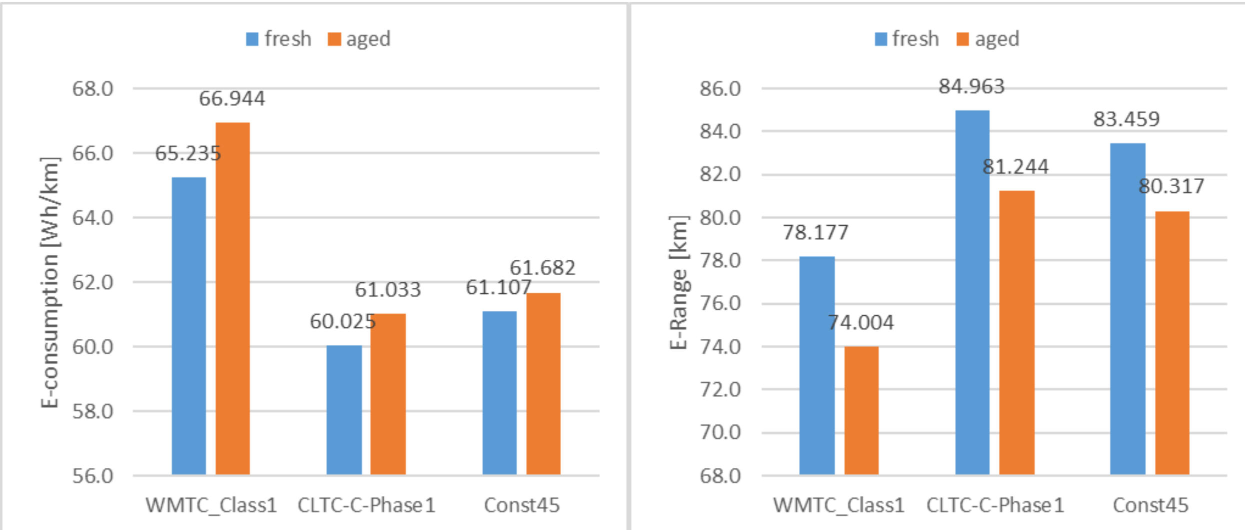

Figure 3-20: Energy consumption and electrical range for fresh and aged cells of 14s10p module and SQ1

When we have a look at the electrical range of SQ1 with two 14s10p battery modules (Figure *3*-20– right), it can be up to 5.2 % for the case of WMTC, and 4.3 % for CLTC vehicle driving cycle. This is due to the combined effect of higher energy consumption, and lower total capacity.

3.4.3 Low-cost approach

To add a low-cost approach for battery aging, a factor for capacity fade k_C and internal resistance increase k_{R_i} is applied to the model, that allows a simplified estimation of the amount of charging and discharging cycle until the performance drops below the defined threshold. *N* is the current status of full cycles. The basic equations are defined as following:

$$C_{aged} = C(1 - k_C \cdot N)$$

$$R_{i,aged} = R_i(1 + k_{R_i} \cdot N)$$

Typical values for capacity fade and internal resistance increase for 25°C ambient temperature due to the different aging process are retrieved from literature and shown in the following Table 3-9: Capacity fade and resistance increase due to cycle aging and calendar aging. In case the battery operates under higher temperatures the effects increase by 2-3 times.

Table 3-9: Capacity fade and resistance increase due to cycle aging and calendar aging

Aging process	Capacity fade rate	Ri increase rate
Cycle Aging	~0.05 – 0.2% per cycle [7]	x3 to x5 at EOL [10]
Calendar Aging	~2 – 5% per year [9] [10]	~10-30% per year of storage [9]
Temperature	Increases the aging by 2-3x [17]	

Using this simple approach allows a quick variation of battery age. One key indicator to evaluate the battery health and remaining lifetime is the SOH, State of Health, it refers to the remaining capacity relative to the original capacity. Adding a simple fading factor that depends on the amount of charging cycles to the nominal capacity of the cell shows a decrease with increasing number of cycles. 5 simulations of different SOHs are conducted: BOL, 40, 80, 120 and 160. Also, a comparison between 25°C and 40°C ambient temperature is done. The current for the simulation is set to 1C.

The results in Figure 3-21 show that after around 160 cycles the capacity decrease is around 2.2% for the 25degC compared to its initial capacity while at 40degC the reduction is 3 times as high, which also aligns with research in this field [17]. The simple model also shows similar degradation to the model in the previous section 3.4.2.

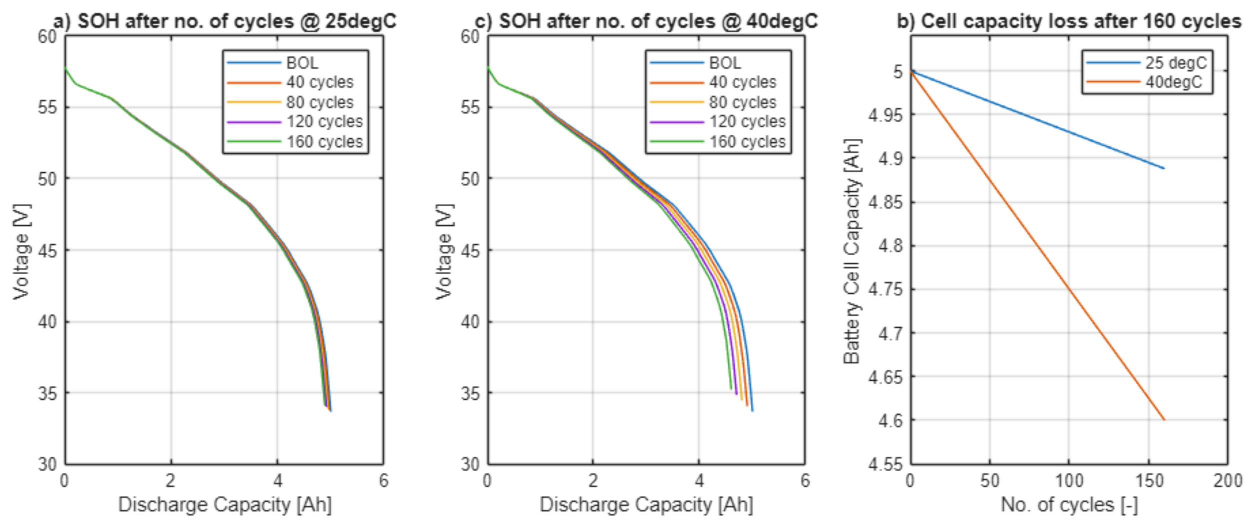

Figure 3-21: SOH assessment between 25degC and 40degC for different no. of cycle using the simple approach

3.5 NVH assessment and lifetime prediction

In this section, the focus is on the *comfort* of the driver, who is directly exposed to noise and vibrations within the vehicle cabin. *Comfort* should be understood in a broad sense: while it is evident that lower levels of noise and vibration are subjectively more pleasant, long-term exposure is also known to have adverse effects on human health [18].

3.5.1 Context and Motivation

Given the target market, price constraints, and intended usage of these vehicles, achieving NVH performance on par with premium-class vehicles is not feasible. Nevertheless, meaningful improvements can still be made. These improvements hinge on two levers: selecting appropriate materials for noise and vibration mitigation, and determining where in the vehicle they can be most effectively applied.

3.5.1.1 Materials for NVH Treatment

In the quest to reduce unwanted noise and vibrations in vehicles, the choice of materials plays a central role. Among the most straightforward strategies used in the automotive industry is to apply lumped acoustic treatments, such as heavy foam panels or layered composites, to the vehicle's interior. These materials offer two main advantages:

- Structural damping – They effectively absorb vibrations transmitted through the body-in-white (BIW), reducing the potential for these vibrations to radiate noise.

- Acoustic absorption – Their porous or multi-layered structure helps dissipate airborne noise, leading to a quieter cabin environment.

However, these materials come with notable drawbacks. Chief among them is their weight, which directly impacts the vehicle's energy efficiency and range — a particularly critical factor for electric vehicles. Additionally, the manufacturing and forming of these treatments can be complex and costly, often requiring custom moulds or manual application steps. As a result, these solutions are typically reserved for high-end or premium-class vehicles, where cost and weight constraints are less restrictive.

In contrast, "frugal" electric vehicles demand NVH solutions that are not only effective but also lightweight, affordable, and easy to industrialize.

This has led to growing interest in the development of materials leading to the so-called metamaterials. Acoustic metamaterials are engineered structures designed to control, direct, or manipulate sound waves in ways not possible with traditional materials. They can exhibit extraordinary properties, such as negative effective mass or modulus, and can be tailored to block or absorb specific frequency bands, including narrow tonal peaks commonly produced by electric drivetrains.

Despite their many advantages, metamaterials are still largely confined to academic research and early-stage industrial demonstrations. Their high manufacturing complexity, sensitivity to defects, and current cost make them ill-suited for mass production in low-cost vehicles. Moreover, scaling their performance over broad frequency ranges and under real-world conditions remains a technical challenge.

As a result, current efforts in frugal vehicle NVH mitigation focus more realistically on lightweight foams, elastomers, constrained layer damping patches, and smart placement of standard materials. Passive components such as rubber bushings also play a critical role, as they can isolate high-frequency vibrations from structural transmission paths, especially between the drivetrain and the chassis.

The challenge, then, lies not only in selecting materials with favourable NVH characteristics but also in deploying them judiciously — achieving the maximum acoustic benefit at the lowest possible cost and weight.

3.5.1.2 Placement Strategies: Prototyping vs. Modelling

Two broad strategies exist to determine where acoustic treatments and vibration isolators should be applied.

The first is prototyping-based. This involves designing an initial vehicle, building a physical prototype, testing its NVH performance, identifying problems, and iterating the design accordingly. While intuitive, this trial-and-error approach is both time-consuming and expensive, requiring significant material and human resources.

The second is modelling-based. Modelling has long been a key tool in engineering. In its early form, it involved simplifying a real object into a basic analytical model — typically one-dimensional — for which hand calculations were possible. Over time, and particularly with the advent of computers since the second half of the 20th century, this concept has evolved into powerful numerical methods that approximate real-world systems with remarkable fidelity.

The underlying philosophy remains the same: represent a complex object as an assembly of simpler subdomains, perform basic calculations on these local elements, and connect them mathematically to approximate the global behaviour of the system. Among the various numerical methods available, the

Finite Element Method (FEM) has emerged as the standard for many kinds of physics simulations, including structural vibrations, acoustics and their coupling: vibroacoustics. FEM allows engineers to discretise the geometry of a component or full assembly into smaller, manageable shapes (typically tetrahedra or hexahedra) and solve the governing physical equations locally across these elements. The aggregation of these local approximations yields a global stable, unique and determinist solution with high accuracy.

In the NVH context, FEM enables prediction of both structural vibrations and the sound they radiate. It allows engineers to test multiple design strategies virtually—well before any prototype is built—and to evaluate their impact on noise and vibration. This approach significantly reduces development cost and effort, making it particularly attractive for low-cost vehicle programs where every iteration matters.

To systematically evaluate the NVH performance of the vehicle and pinpoint the most critical transmission paths and weak spots, we will rely on FEM simulations. This approach enables a detailed analysis of both structural vibrations and the resulting acoustic field within the cabin. In the following section, we introduce the governing equations used to model structural dynamics and acoustic propagation, which form the foundation of our simulation framework.

3.5.2 Theoretical background

As the acronym NVH suggests, the problems at hand rely on two physical phenomena: i) acoustics, and ii) structural vibrations. Both phenomena fall into the category of so-called *wave problems*. Before introducing the governing equations, we can already take advantage of the wave-like nature of these phenomena.

While it is natural for humans to reason and analyse in the time domain, time-dependent equations are often more difficult to handle mathematically. Fortunately, the genius of Joseph Fourier lies in having demonstrated that any temporal signal (and by extension, many physical phenomena) can be expressed as a linear combination of wave functions of different wavelengths or frequencies. This foundational result enables physicists and engineers to work in the *frequency domain*, where the behaviour of linear time-invariant systems often becomes much simpler to describe and analyse.

In the following, all equations are expressed in the frequency domain using the $e^{-\mathrm{i}\omega t}$ time convention, where i is the pure imaginary number, ω is the angular frequency related to the frequency by $\omega = 2\pi f$, and t is the time variable.

3.5.2.1 Governing equations

Let us first introduce the governing equation of acoustics. Consider a fluid domain in which the speed of sound is denoted by c. What the human ear perceives as *sound* corresponds to small pressure fluctuations around the ambient (atmospheric) pressure. We denote this fluctuation by p, called the **acoustic pressure** (measured in pascals, Pa). It is important to note that p is a scalar field. In, under the assumptions of linear acoustics and time-harmonic excitation, the acoustic pressure satisfies the **Helmholtz equation**:

$$\Delta p + \left(\frac{\omega}{c}\right)^2 p = 0$$

where $\Delta \cdot$ denotes the Laplacian operator. This equation is an elliptic partial differential equation, it can be solved analytically for a handful of academic cases, but for more elaborate ones (such as the ones we are facing) it is not possible and using computational methods is mandatory.

Concerning structural vibrations, we introduce a structural domain Ω_s. What we call **vibrations** are small displacements (or oscillations) of the solid's particles around their equilibrium positions. This displacement is commonly denoted by the vector field u, which can be expressed as:

$$u = \begin{pmatrix} u_x \\ u_y \\ u_y \end{pmatrix},$$

where u_x, u_y, and u_z are the components of the displacement vector u in the chosen coordinate system, preferably orthonormal.

The governing equation is derived from the local application of Newton's second law of motion and, in the frequency domain, takes the general form:

$$\mathrm{div}\sigma + \rho_s \omega^2 u = F_{ext}$$

where σ is the stress tensor, ρ_s is the material density, F_{ext} is the external force per unit volume.

This partial differential equation expresses the balance between internal forces (modelled via spatial derivatives), external excitations and acceleration. Like the Helmholtz equation for acoustics, it generally cannot be solved analytically for real-world geometries, and must be tackled numerically — notably using the Finite Element Method.

In vibroacoustic problems, we consider both an acoustic domain Ω_f and a structural domain Ω_s. Each domain is governed by its respective equation — the Helmholtz equation for acoustics and the elastodynamic equation for structural vibrations. However, on the interface $\Gamma = \partial\Omega_s \cap \Omega_f$ where the two domains meet, they interact. Two physical continuity conditions must be satisfied at this interface.

1. **Continuity of normal displacement** (or displacement velocity in time domain): This condition ensures that no vacuum forms and no matter instantaneously disappears at the interface:
$$\frac{\partial p}{\partial n} = -\omega^{2\rho_f} u \cdot n,$$
where n is the outward-pointing normal vector of the structural domain and ρ_f is the fluid density.

2. **Continuity of effort** (Newton's third law, or action-reaction principle): This condition ensures that the pressure applied by the acoustic fluid on the structure equals the normal stress applied by the structure on the fluid. It reads:
$$\boldsymbol{\sigma} \cdot \boldsymbol{n} - p\boldsymbol{n} = 0,$$
where σ is the stress tensor in the solid.

These two conditions create a bidirectional coupling: structural vibrations influence the acoustic field, and vice versa. This coupling must be handled carefully when solving vibroacoustic problems numerically, typically via FEM or FEM-BEM (Boundary Element Method) methods.

For linear, time-invariant wave problems — such as those encountered in acoustics and structural vibrations — the principle of **reciprocity** holds. Simply stated, reciprocity means that the response at point A due to a unit source at point B is equal to the response at point B due to an identical source at point A.

This property can be exploited to simplify simulations: by computing the response in many positions for a single source location, reciprocity allows us to infer the response at that same point if the source were moved to different locations. This avoids the need to solve multiple problems with different right-hand sides, or to perform extensive additional measurements — ultimately reducing both computational and experimental effort.

3.5.2.2 The Finite Element Method in 3 paragraphs

In this small section, we lay out the basic concepts behind the Finite Element Method (FEM). We will not go into the mathematical details or algorithms at the root of FEM, as this would fall outside the scope of the present report. For instance, any FE model relies on a so-called weak form, which is a bilinear equation obtained by applying a weighted residual scheme to the governing equations. The interested reader can refer to [19] and [20] for a complete mathematical treatment. However, it is important to grasp the underlying philosophy of FEM.

FEM relies on three key components: i) a discretization of the domain of interest into small, simple shapes (triangles, quadrilaterals, tetrahedra, or hexahedra), called elements; the collection of these elements forms a mesh; ii) a local polynomial approximation of the solution on each element; iii) the definition of boundary conditions.

The theory associated with the polynomial approximation is mathematically involved, and will not be detailed here. It is sufficient to keep in mind that results obtained through FEM are approximate, and take the form of continuous fields defined element-wise, using polynomials. As for meshes and boundary conditions, rather than introducing them abstractly in this theoretical background, they will be presented concretely in the analysis section through practical examples.

3.5.3 Analysis

In this section, we present the NVH analyses carried out. All analyses have been performed on the vehicle developed by TUX Mobility, shown in Figure 3-22.

Figure 3-22: TUX mobility vehicle

All analyses in this section rely on FEM. Naturally, this requires the use of meshes. Meshes are always generated from a CAD (Computer Aided Design) model of the product, which is essentially a 3D digital representation of the vehicle. For confidentiality reasons, the CAD model itself cannot be disclosed here.

In the following, whenever the term "CAD model" is mentioned, simply think of it as a computer-readable 3D representation of Figure 3-22.

3.5.3.1 Acoustic simulations

We begin with the acoustic models. The objective of this analysis is to determine the acoustic comfort in the driver cabin and to provide a methodology that could later be used to improve comfort at targeted frequencies. For the present report, the frequency range of interest is chosen to be:

$$f \in [20\text{Hz}, 1000\text{Hz}].$$

In line with the frugal philosophy of the project, the analysis does not focus on acoustic levels throughout the entire cabin, but rather on the sound pressure in the vicinity of the driver's ears — the primary region affecting perceived comfort.

This initial study is purely acoustic and limited to design modifications that the OEM can realistically implement at this stage. Aeroacoustics effects (which are largely driven by the vehicle's exterior geometry) are not considered, nor are major changes to the geometry envisaged as a means of improving comfort. The focus is set on noise radiated by structural panels into the cabin.

A practical way to estimate how a particular structural point contributes to noise at the driver's ear is to place a monopole source at that point and compute the resulting sound pressure at the driver's ear location. Repeating this operation for many points on the structural surface in contact with the acoustic domain yields valuable insight into structure-borne noise as perceived by the driver — as will be shown in the following.

As previously mentioned, all such analyses are performed using the Finite Element Method (FEM), which first requires the construction of an acoustic mesh.

3.5.3.1.1 Mesh

To mesh an acoustic cavity, a representation of the surface enclosing the cavity — often referred to as the "outer skin" — is needed. As can be seen in Figure 3-22, the driver cabin is open on both sides. This implies that, in practice, the acoustic domain is infinite and does not have a well-defined outer skin. To address this, artificial boundary surfaces must be added at the open sides, and special numerical treatments will later be applied on these surfaces. For these treatments to perform optimally, it is important that the added surfaces are not "too concave", meaning they should avoid sharp edges pointing into the acoustic domain.

Once this watertight outer skin is defined, meshing can proceed. When meshing an acoustic domain, one must carefully consider the element size relative to the smallest wavelength of interest. The smallest wavelength corresponds to the highest frequency. In this case, the upper frequency limit is 1000 Hz, which yields a wavelength:

$$\lambda_{\min} = \frac{c}{f_{max}} = \frac{340}{1000} = 0.34\text{m}.$$

Traditional low-order elements typically require ~6 points per wavelength (about 5 elements). However, when using High-Order FEM [21]— as we do here — this requirement can be relaxed to some extent. In our case, we employ High-Order FEM with adaptive polynomial order, with an upper bound of order 10.

With 10th-order elements, we obtain 11 points per element (per direction), which means elements of ~34 cm are sufficient to resolve a wavelength.

However, as one can glimpse from Figure 3-22, many geometric features in the cabin are significantly smaller than 34 cm. If we used elements of that size, we would approximate the geometry very poorly. Clearly, in this case, element sizing is driven by geometric fidelity. The mesh must capture the geometry accurately enough to avoid introducing errors from the geometry itself.

For this reason, the element size was tuned accordingly. In the present study, the maximum element edge length was set to 1 cm close to geometric details, resulting in the mesh shown in Figure 3-23.

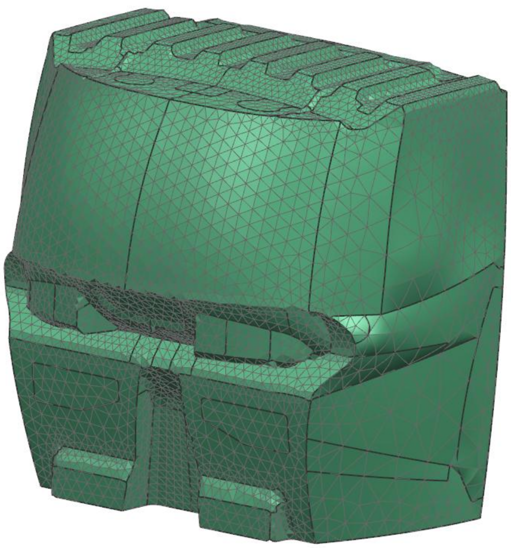

Figure 3-23: Acoustic mesh with h = 1cm close to geometric details.

3.5.3.1.2 Boundary conditions

Now that the mesh is obtained, boundary conditions must be defined. Three types are needed in this case: i) on the outer skin in contact with the structure panels, ii) the monopolar source, and iii) the previously mentioned *special treatment* on the open ends of the cabin.

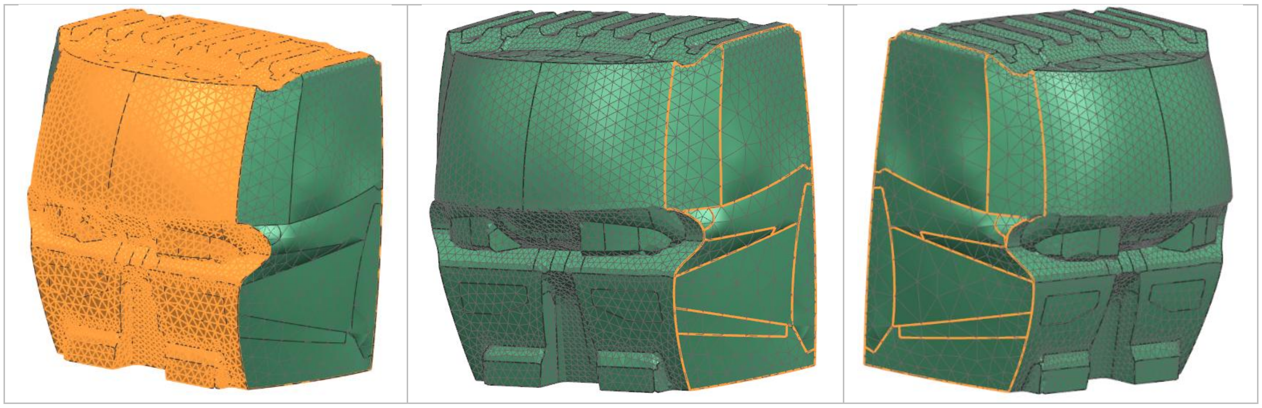

Figure 3-24: Different physical regions of the acoustic mesh. From left to right:a) Surface in contact with structure panels; b) Left hand side open end;c) Right hand side open end.

Let us begin with the surfaces in contact with the structure panels; this group of surfaces is highlighted in orange in Figure 3-24 a). Since no damping treatments such as padding, foam, lumped masses or carpets are currently implemented in the cabin, these surfaces are assumed to be rigid. The rigid wall boundary condition is prescribed by enforcing a null acoustic velocity:

$$\frac{\partial p}{\partial n} = 0.$$

This is the natural (i.e., homogeneous Neumann) boundary condition of the weak form of the Helmholtz equation — in other words, the system matrix remains unchanged.

Next, we address the monopolar sources. As previously explained, the goal is to estimate the pressure at the driver's ear resulting from a monopole located at various points on the structure panels. This would naively require placing a monopole at position X_1, solving the problem, measuring the result at point M(driver's ear), then repeating for X_2, X_3, etc., which quickly becomes computationally expensive.

Instead, all this information can be obtained from a **single** solve by leveraging the reciprocity principle. Indeed, the pressure at M induced by a monopole at X_1 is equal to the pressure at X_1 induced by a monopole at M. So, by placing a monopole at the driver's ear and computing the acoustic pressure on all the vertices of the orange triangles in Figure 3-24 a), we effectively retrieve the desired pressure values at the ear due to many different source locations on the structure.

Finally, we turn to the *special treatment* needed at the open ends of the cabin, highlighted in orange in Figure 3-24 b) and Figure 3-24 c). On these artificial surfaces, we must ensure that outgoing waves are not reflected back into the acoustic domain. Several techniques exist to achieve this, but the most widely used is the Perfectly Matched Layer (PML) [22]. The PML consists of a buffer region composed of additional elements where the spatial coordinates are stretched into the complex plane. This transformation turns propagating waves into evanescent ones, which are then exponentially damped. Conceptually, the PML acts as a *numerical sponge* that absorbs outgoing waves.

In practice, using classical PMLs can be tedious, particularly in complex geometries. For that reason, Automatic Matched Layers (AML) [23] are often preferred. AMLs automatically extrude the necessary elements from the designated surfaces. This is why the added surfaces must be convex or at least not *too concave*, as overly concave regions can interfere with the AML extrusion process.

3.5.3.1.3 Results and discussion

The system defined above is solved at different frequencies lying in [20Hz, 1000Hz]. Given this relatively wide frequency range, there is no need for a very fine frequency resolution — a resolution of 2~Hz is more than sufficient to identify the system's resonant frequencies. For clarity, the system is solved at the following discrete frequencies:

$$f = [20\text{Hz}, 22\text{Hz}, 24\text{Hz}, \dots, 1000\text{Hz}].$$

One might argue that resonant frequencies could be obtained more directly by performing an eigenvalue analysis. However, several reasons motivate the choice to avoid this approach:

- Performing an eigenvalue analysis up to 1000~Hz on such a large system would require substantial computational resources.

- Since our focus is limited to the pressure at the driver's ear, computing full eigenvectors (which provide information throughout the cabin) would be inefficient and unnecessary.
- The AML (Automatic Matched Layer) is frequency-dependent, which complicates eigenvalue computations. While certain research methods exist to address this [24], they remain challenging to apply to industrial (non-academic) systems, computationally demanding and can be difficult to stabilize.

Examples of computed pressure fields at selected frequencies are provided in Figure 3-25.

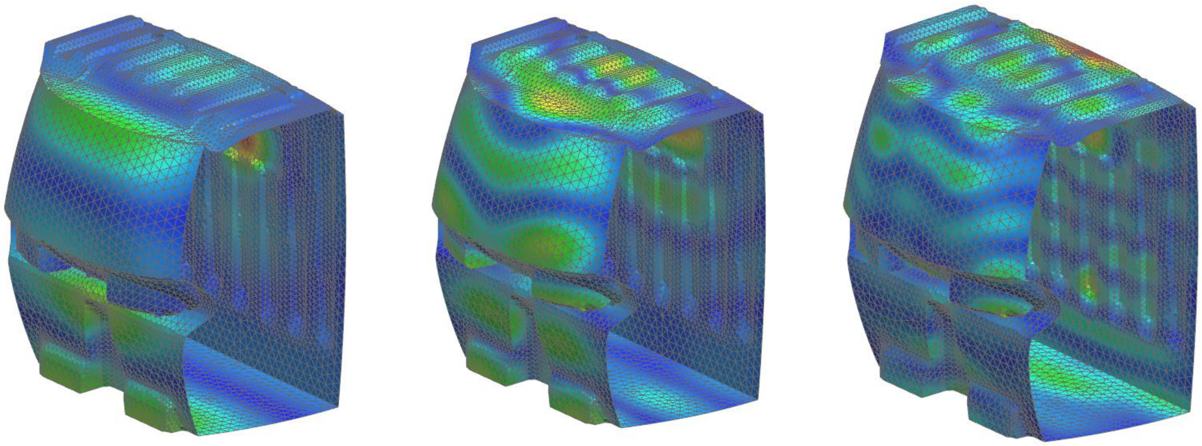

Figure 3-25: Example of pressure fields at different frequencies. From left to right: 196Hz, 616Hz, 936Hz.

In Figure 3-26-left, we plot the acoustic pressures at the driver's ear (resulting from each monopole on the structure, via reciprocity) versus frequency, this type of curve is called a Frequency Response Function (FRF). The red curve represents the maximum value at each frequency step. This curve can be interpreted as a *worst-case scenario*: by reasoning on this conservative curve, we ensure conservative design decisions.

For improved readability, Figure 3-26-right shows the same red curve, but with a different ordinate range to better highlight the relevant trends.

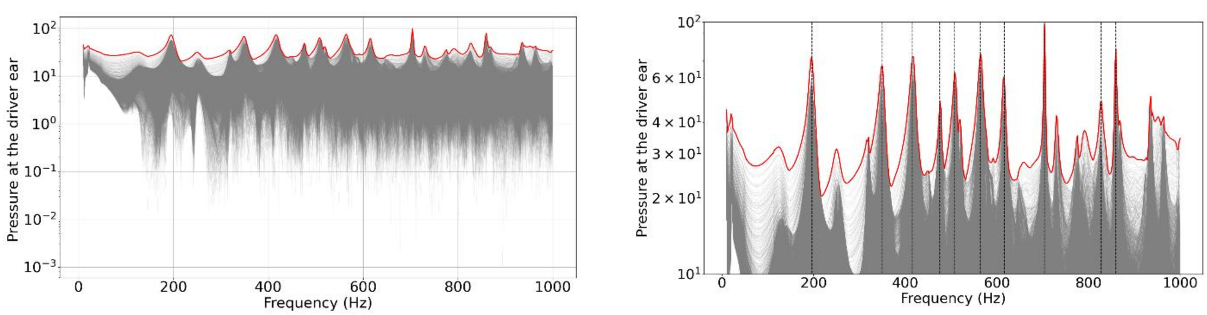

Figure 3-26: FRF at the drivers ear.

The red curve in Figure 3-26-right exhibits numerous variations, among which several stand out clearly as sharp peaks. The frequencies at which these peaks occur are referred to as *resonant frequencies*, and they are highlighted with vertical dashed lines.

To clarify: if there is any source exciting the system at one of these frequencies, the system will *resonate*, and the noise level perceived by the driver will become very high — even if the source itself is not particularly intense. Therefore, when aiming to improve the NVH behaviour of the system, efforts should focus on reducing these peaks.

For completeness, the values of the resonant frequencies are reported below in Table 3-10.

Table 3-10: Resonant frequencies perceived at the driver's ear.

Number	1	2	3	4	5	6	7	8	9	10	11
Value (Hz)	196	350	416	476	508	564	616	704	828	860	936

It is also worth noting that at low frequencies (around 20 Hz), even though there is no sharp peak, the acoustic levels remain relatively high. In this work, we *ignore* this aspect because improving comfort at such low frequencies typically requires solutions that are not compatible with the frugal philosophy of this project (e.g., thick lumped mass padding).

We now lay out a method to improve the acoustic comfort in the cabin. The track pursued here is: adding a carpet-like lining on (at least) one of the surfaces of the cavity. We chose the back surface of the domain — see the orange highlighted area in Figure 3-27. One could have chosen another surface; we selected this one because it offers the largest area and, from a practical perspective, is less prone to wear and tear compared to the floor.

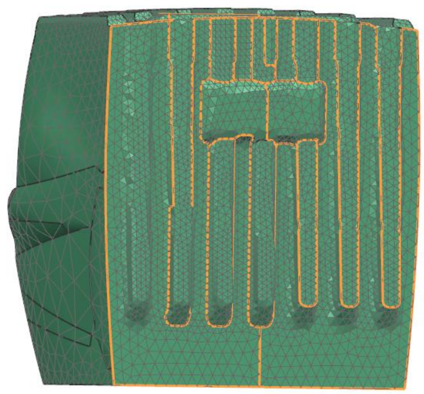

Figure 3-27: Back surface of the cabin where the lining is added

To account for this lining in the model, an acoustic impedance boundary condition is imposed on the appropriate surface. The impedance, denoted Z, is a complex, frequency-dependent quantity that captures the idea of sound absorption. Choosing the right carpet (density, thickness, etc.) should be done based on the targeted frequency range and in consultation with material suppliers that the OEM prefers to work with.

For the sake of this example, we use the material discussed in [25], whose properties are shown Figure 3-28. As can be seen on the absorption curve, this material performs best between 600~Hz and 900~Hz, which lies within our frequency range of interest.

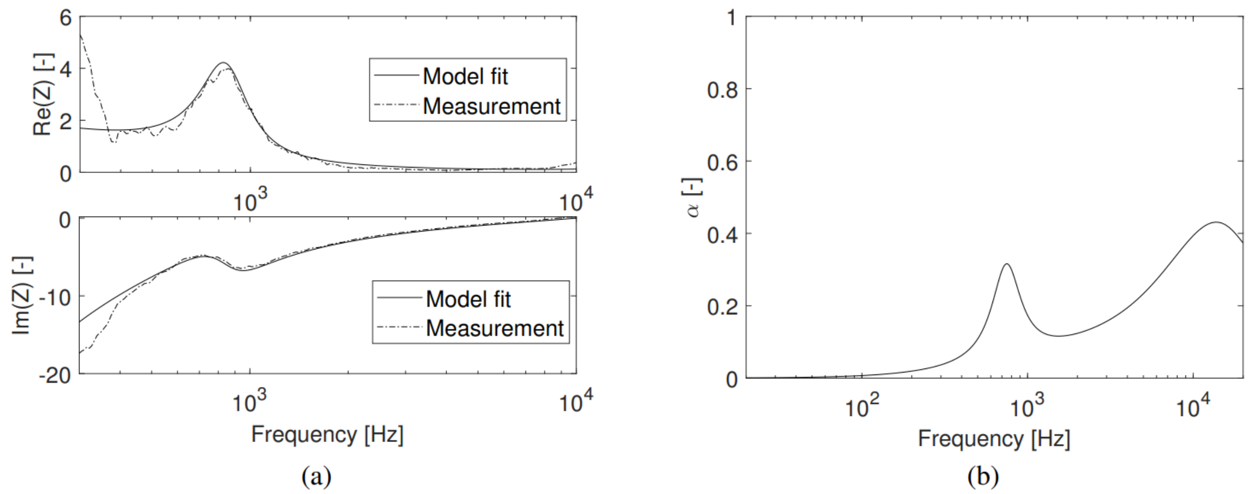

Figure 3-28: Acoustic properties of the carpet lining. Top left: Real part of the impedance; Bottom left: imaginary part of the impedance; Right: absorption.

After applying this modification, the system is solved again. The new FRFs are plotted in Figure 3-29, where the maximum curve is highlighted in blue. For clarity, the maximum FRF of the untreated system (in red) and the maximum FRF of the system with the carpet lining (in blue) are plotted together in Figure 3-30.

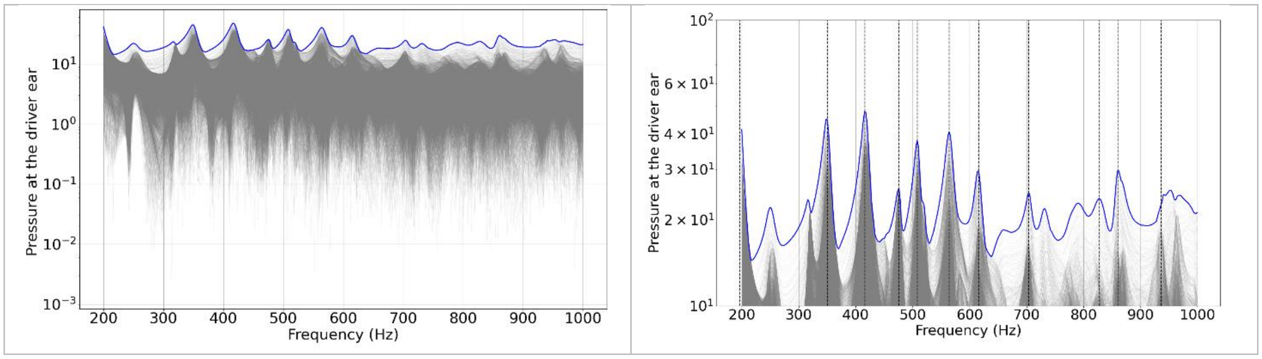

Figure 3-29: FRF at the driver's ear with acoustic lining

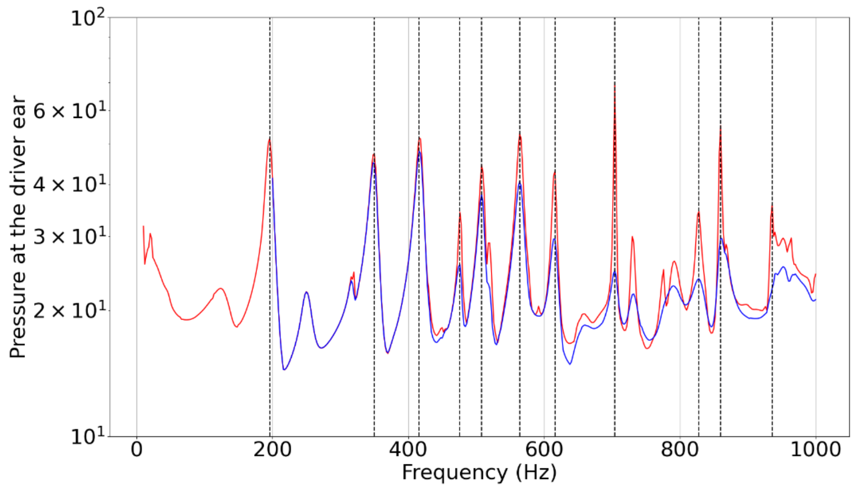

Figure 3-30: Comparison of FRF. Red: without acoustic lining; Blue with acoustic lining

As expected, Figure 3-30 shows a clear reduction of the acoustic levels in the frequency band where the carpet material is most effective (approximately 600~Hz to 900~Hz). This confirms that even simple, frugal modifications — such as adding a lining on an appropriate surface — can meaningfully improve perceived acoustic comfort. This concludes the acoustic study; in the following sections we will consider the vibration aspects.

3.5.3.2 Structure vibration analysis

We now address vibration mitigation, focusing on a purely structural approach. In keeping with the project's frugal philosophy, the objective is not to monitor or mitigate vibrations across the entire structure but to act locally on areas where improvements will have the greatest impact on the driver's comfort. The primary source of vibrations considered here is the electric drivetrain. As in the acoustic study, the Finite Element Method (FEM) will be employed, and the same sequence will be followed: i) mesh; ii) boundary conditions and connections; iii) solving and analysis.

3.5.3.2.1 Mesh

Let us begin with a non-formal note on FEM computational cost. The number of mesh nodes directly drives the size of the system matrices, and thus the simulation's computational cost. In acoustic problems, the primary unknown — pressure — is a scalar field, so the matrix size is equal to the number of nodes. In structural problems, however, the displacement field is a three-component vector (cf section 3.5.2.1), meaning the system matrices are roughly three times larger for the same number of nodes. For this reason, keeping the node count as low as possible is key.

The vehicle's structural frame (see Figure 3-33) consists mainly of tubular beams whose typical cross-sections are shown in Figure 3-31; standardized dimensions for such beams can be found in manufacturers' catalogue.

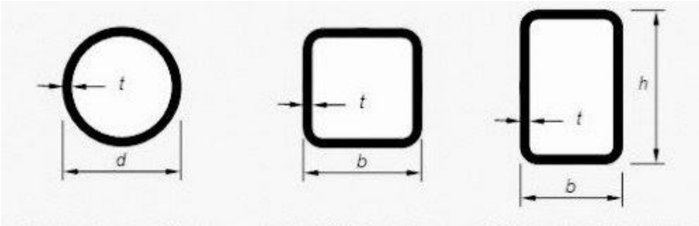

Figure 3-31: Cross section of tubular beams

Meshing the entire frame with 3D solid elements would result in an excessive number of nodes and prohibitively expensive computations. Fortunately, appropriate simplifications can be made without degrading the quality of the results. Since our interest lies in vibrations transmitted from the electric drivetrain to the driver's seat — a distance on the order of ~1m. To remain in the domain of legitimate operation of FEM, given the size of the vehicle, the shortest wavelength considered should not be smaller than a couple of centimetres. Bellow that threshold the study would fall in the *high-frequency* range, where FEM do not apply, and one need to resort to statistical methods such as the Statistical Energy Analysis [26]. The typical thickness t of a tubular beam is a few millimetres, so:

$$t \ll \lambda$$

no significant through-thickness variation of the vibration field is expected in our frequency range of interest. It is therefore justified to model the frame using 2D shell elements, avoiding the need to mesh through the thickness, see Figure 3-32.

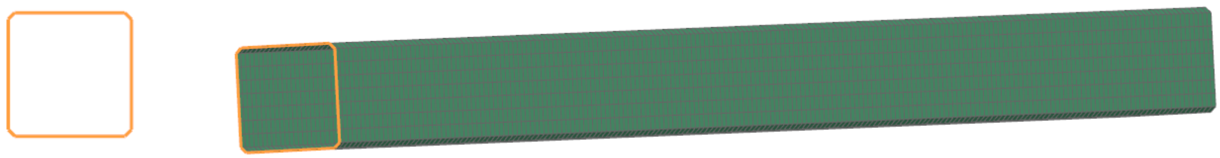

Figure 3-32: Example of a beam meshed with 2D elements. Leftt: view perpendicular to the beam direction; Right: view of the whole beam.

The resulting mesh is shown in Figure 3-33. As can be seen, some parts — notably the engine mounts — are meshed with 3D solid elements. This is done to more accurately represent boundary conditions and connections at those key interfaces.

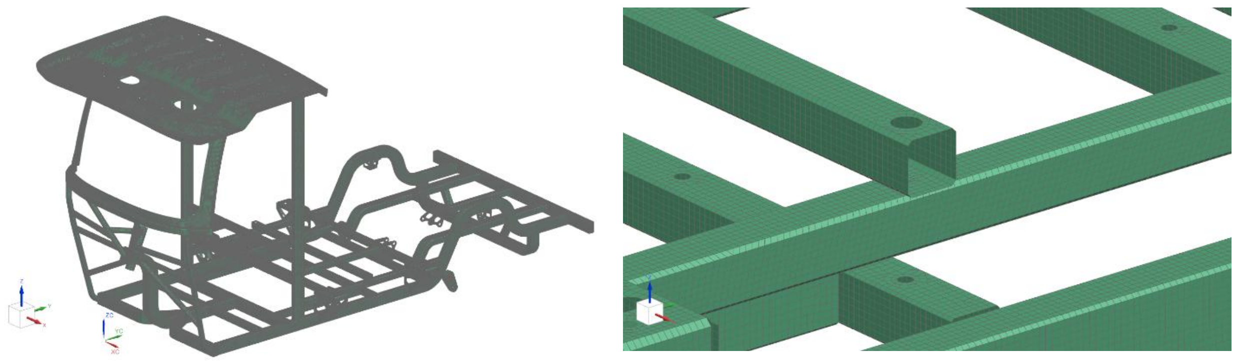

Figure 3-33: Mesh of the TUX mobility vehicle. Left: entire mesh; Right zoom on a group of beams.

An important component is still missing from the mesh: the engine. Unfortunately, no CAD model of the engine was available at this stage. However, since the objective here is to evaluate vibrations transmitted to the vehicle structure — and not the detailed internal dynamics of the engine — it is sufficient to model the engine as a rigid body. In the mesh, the engine is represented as a simplified rigid body, visualized as four connected lines in Figure 3-34-Left.

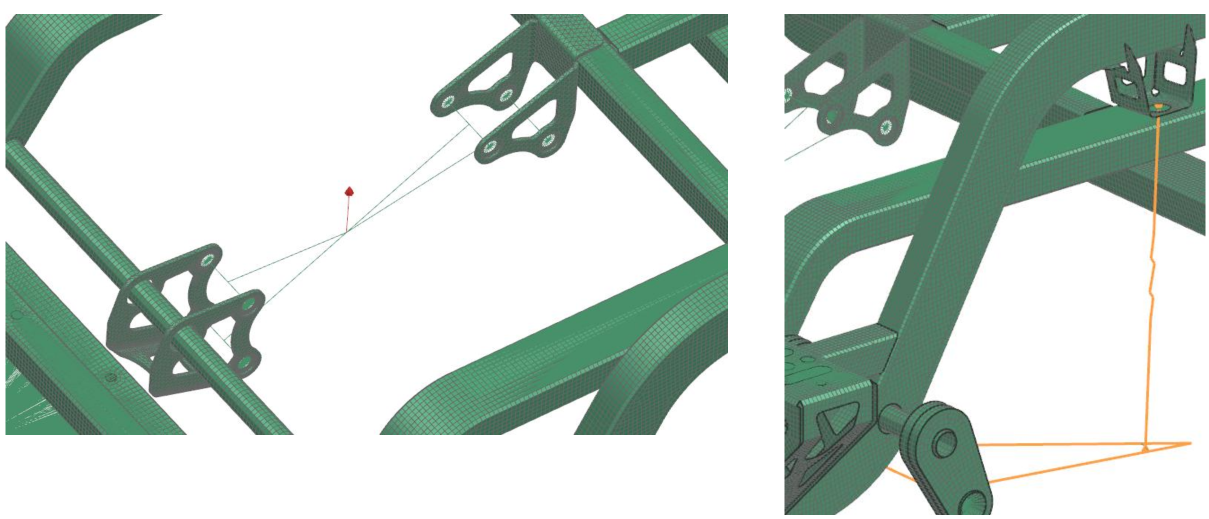

Figure 3-34: Left: engine represented as a rigid body; Right: suspensions linkage represented as a spring and rigid beams.

Similarly, the suspension system is not modeled in full detail. To reduce computational cost, it is represented using a linkage of rigid elements (REB2) combined with 1D spring elements, as shown in Figure Figure 3-34-Right.

3.5.3.2.2 Boundary conditions and connections

Up to this point, we have only meshed the components of the assembly; none of the parts are yet connected to one another. This step now needs to be addressed. In this assembly, we distinguish two main types of connections: welds and bolted joints.

Concerning welds: a weld essentially *bonds* one part to another across their mating surfaces. Since the goal here is not to study stress distributions or concentrations in the weld itself, it is unnecessary to explicitly model the added lip of weld material. It is sufficient to apply a *gluing* condition between the mating interfaces. This condition works by taking each node on the mating interface of part A, finding the closest neighbouring node on part B, and enforcing a constraint equation that ensures both nodes undergo identical displacements. This operation is repeated for every node belonging to the interface. An example is illustrated in Figure 3-35.

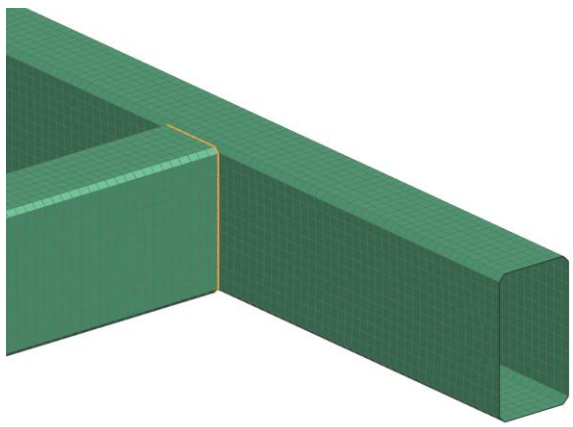

Figure 3-35: Two beams glued along the orange edges.

Concerning bolted joints: these can be modelled in various ways. If the objective were to analyse stress concentrations, possible separation or sliding, or bolt preload effects, a detailed nonlinear model representing the full bolt geometry (bolt + washer + nut) would be necessary. However, such nonlinear models are computationally costly and of little added value in the present context, where the goal is to capture the global dynamic behaviour of the structure.

A much simpler and computationally efficient approach is to use REB2 elements. A REB2 (Rigid Element Beam 2-node) is a massless beam element that transmits all degrees of freedom between two nodes. It behaves as an infinitely stiff connector, enforcing both translational and rotational continuity between its end nodes. In other words, the two connected nodes will experience identical translations and rotations. This provides a good approximation of a rigid bolted joint under the small displacement and linear vibration assumptions of this study, and is perfectly suited for the current analysis.

To model bolted connections using REB2 elements, a node N1 is created at the centre of the circular hole in part A. This node N1 is connected via REB2 elements to all the nodes along the circumference of the hole in part A, effectively rigidifying the local region around the bolt. The same operation is performed on part B, creating a node N2 similarly connected to the circumference of the hole in part B. Finally, a single

REB2 element is added between N1 and N2, thereby completing the representation of the bolted connection.

Now that the model is fully connected, boundary conditions need to be defined. Since the problem at hand involves an assembly, let us stress that boundary conditions here refer to the external loads and constraints applied to the structure as a whole.

As mentioned earlier, the goal is to study vibrations induced by the electric drivetrain. Because the drivetrain is modelled as a rigid body, its vibrations are simulated by applying a harmonic point force at its centre of mass, as shown in Figure 3-34-Left.

However, applying this external force alone is not sufficient to obtain a solvable system: the entire assembly would still be free to translate and rotate along certain axes, resulting in a singular (non-invertible) system matrix. To resolve this, appropriate degrees of freedom (DOFs) are constrained at the wheel hubs, effectively anchoring the assembly while still allowing it to respond to excitation.

3.5.3.2.3 Results and discussion

To monitor vibrations perceived at the driver's seat, an approach similar to the one used in the acoustic section could be employed: namely, apply a known point force to the engine and measure the vertical displacement at the driver's seat across the frequency range. However, with a slightly different method, we can obtain results that are more directly linked to real-world driving conditions.

When an electric motor runs at a given RPM, the vibrations it produces in the time domain can be expressed as a linear combination of sinusoidal functions. In other words, by performing a Fourier transform on the measured acceleration signal as the motor revs, one can identify the dominant frequencies present at each RPM.

Typically, this is visualized as a map such as Figure 3-36, where the vertical axis is RPM, the horizontal axis is vibration frequency, and the colour represents vibration amplitude. With such a map, we can quickly identify which frequencies are dominant for each RPM. Note: The data presented here is anonymized; the absolute values are not important — we are simply illustrating the methodology.

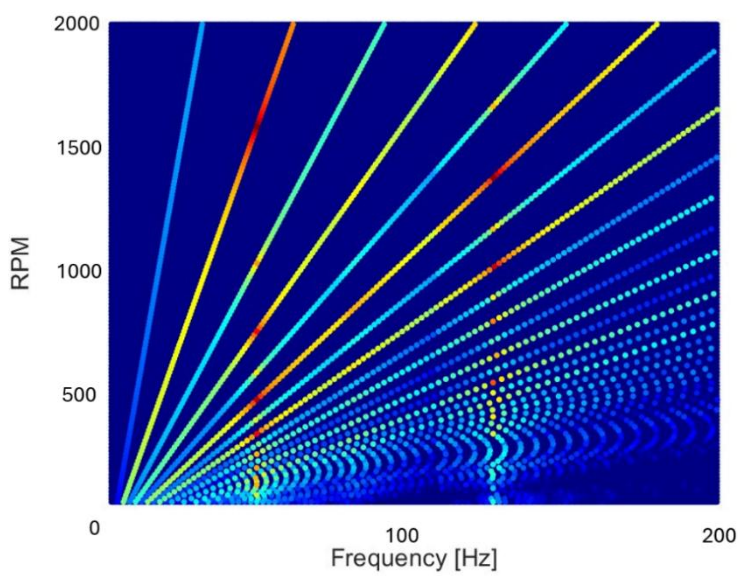

Figure 3-36: RPM vs Frequency vs amplitude of vibrations of the engine (anonymized)

To reduce the number of required structural simulations, we can choose to focus on the RPM range where the engine is expected to operate most of the time. For this example, we assume this value is 1500 RPM. The associated dominant frequencies and their amplitudes are provided Table 3-11.

Table 3-11: Amplitude of vibration of the engine at different frequencies at 1500rpm (extracted from Figure 3-36)

Frequency (Hz)	20	45	65	100	120	140	158	180
Amplitude (mm)	**.1**	**1**	**.2**	**.4**	**.2**	**.8**	**.15**	**.4**

Table 3-11 should be interpreted as follows: at 1500 RPM, the engine will excite the structure at 20 Hz with an amplitude of 0.1, at 45 Hz with an amplitude of 1, and so on. Thanks to the linearity of the system, the resulting displacement at the driver's seat can be computed by superposing the individual displacements: it is the sum of the displacement at 20 Hz (scaled by 0.1), plus the displacement at 45 Hz (scaled by 1), and so forth. This avoids the need to solve the system for every frequency in the full RPM range.

This is demonstrated here on our example system. Example displacement fields at the driver's seat are shown in Figure 3-37.

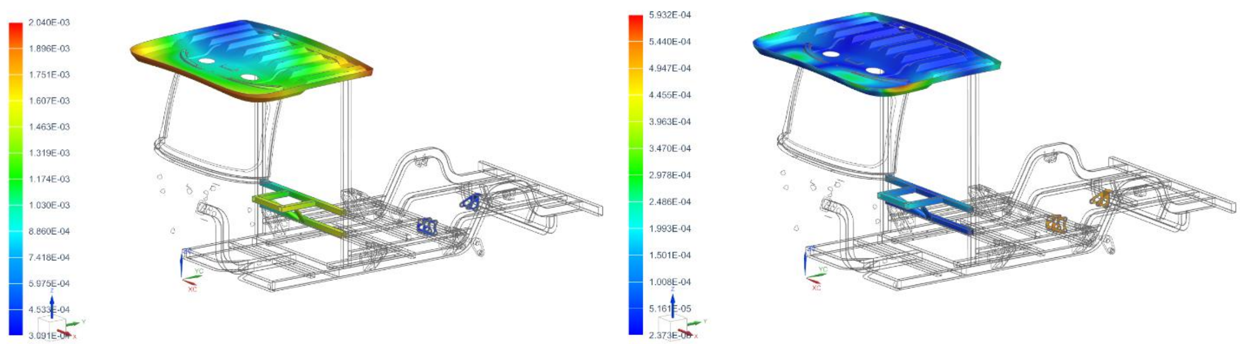

Figure 3-37: Example of displacement fields at 20Hz (left) and 158Hz (right).

Table 3-12: Table with values to obtain the displacement at the driver seat for a cycle of 1500rpm

Frequency (Hz)	20	45	65	100	120	140	158	180
Engine Amplitude (mm)	**.1**	**1**	**.2**	**.4**	**.2**	**.8**	**.15**	**.4**
Seat amplitude for unit input (mm)	0,0029	0,00026	0,001	0,0354	0,00068	0,007	0,0001	0,00013
Scaled seat amplitude (mm)	.00029	.00026	.0002	.01416	.000136	.0056	.000015	.000052
Amplitude of vibration at driver seat at 1500rpm (mm)	**0,020713**							

Table 3-12 summarizes the key data for this analysis:

- the dominant frequencies at 1500 RPM;

- the amplitude of engine excitation at those frequencies;
- the displacement at the driver's seat per unit input force at those frequencies;
- the product of the previous two columns (the actual contribution to displacement);
- the sum of those contributions, i.e. the total vibration amplitude at the driver's seat at 1500 RPM.

From these results, OEMs can make informed design decisions and identify areas for improvement. The main levers for reducing vibration would be:

- selecting an appropriate engine mount — typically a rubber bushing that dampens vibrations in a frequency-dependent manner — so it should be chosen carefully;
- similarly, adding compliant or damping layers between the seat and the structure (such as rubber pads) can further mitigate transmitted vibrations.

In summary, this initial structural analysis provides a clear view of how vibrations from the electric drivetrain propagate to the driver's seat across relevant operating conditions. By linking engine RPM to the dominant vibration frequencies — as observed in real-life usage — the approach remains closely connected to actual driving scenarios. Combined with a simplified yet representative structural model (using beam elements, rigid-body approximations, and appropriate connection strategies), this method offers computational efficiency and actionable insights. With this baseline established, we can now move on to the next step: evaluating how these dynamic loads translate into structural fatigue and long-term durability.

3.5.3.3 Fatigue analysis

We now switch focus from vibrations to fatigue analysis. The objective is to anticipate potential failure due to the accumulation of microscopic damage under cyclic loads. Among the components of the vehicle, the solar panel mounted on the roof is identified as one of the most critical with respect to fatigue: it is continuously exposed to dynamic excitations — notably road-induced vibrations transmitted through the structure — and its function (energy harvesting) is essential.

However, since the detailed CAD model of the solar panel was not available at this stage, the present analysis is carried out on the mounting plate to which the panel is attached. This plate serves as the interface between the roof structure and the solar panel, and its fatigue behaviour is key to ensuring the long-term structural integrity of the entire assembly.

The fatigue analysis is performed leveraging the Dirlik method [27], a well-established approach for predicting fatigue life under random vibrations. Instead of requiring a time-domain history of stresses, which may be difficult to obtain or process for long usage scenarios, the Dirlik model operates on the **Power Spectral Density (PSD)** of stress. From this, it estimates the distribution of stress cycles in the material, which can then be combined with the S-N (Wöhler) curve of the material to compute damage accumulation. This method provides a computationally efficient way to assess fatigue life, particularly well-suited to random, broad-band excitations such as those encountered in vehicle structures.

The structural mesh developed previously is reused here in its entirety — no new model needs to be developed. This ensures both consistency across the analyses and computational frugality.

It is important to stress that the PSD of excitation used in this analysis is strongly road-dependent. Different types of road surfaces — smooth asphalt, cobblestones, dirt tracks — generate different vibration profiles, both in amplitude and in frequency content. As a result, the fatigue predictions obtained with this methodology will vary greatly depending on the intended usage profile of the vehicle. For example, a vehicle used primarily in urban environments will experience a very different fatigue loading than one used in rural settings with frequent off-road segments. It is thus essential to carefully select or measure representative road profiles for each target use case when performing this kind of analysis.

Road-induced vibrations are typically low-frequency [28]. Consequently, in this study we limit the frequency range to:

$$f \in [1\text{Hz}, 30\text{Hz}].$$

In this analysis, we consider the road profile shown in Figure 3-38. This plot provides statistical information on the amplitude and frequency of vibrations transmitted through the wheels. It is important to stress that such a curve is strongly dependent on the type of road surface. However, in order to perform a fatigue analysis, we need the PSD of the stress in the component of interest.

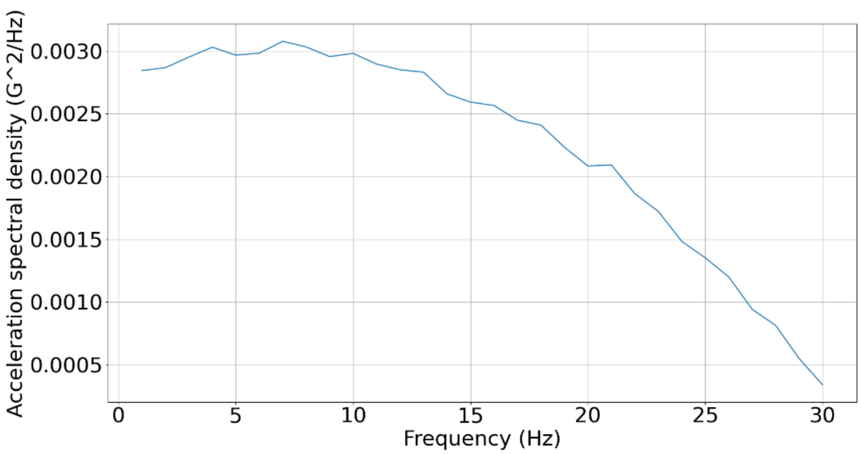

Figure 3-38: Power spectral density of the acceleration of the road.

3.5.3.3.1 From road profile to component stress

We now describe the procedure used to derive the PSD of the stress experienced by the solar roof, starting from the PSD of the road profile given in Figure 3-38. The method proceeds as follows:

- Solve the structural model for a unit acceleration applied at the wheel hub, for each frequency where the acceleration PSD is defined.
- For each frequency, compute the maximum stress experienced by the solar roof.
- Scale the maximum stress at each frequency using the corresponding amplitude of acceleration given in Figure 3-38.

This process yields the PSD of the stress in the part. The resulting stress PSD for the present case is shown in Figure 3-39.

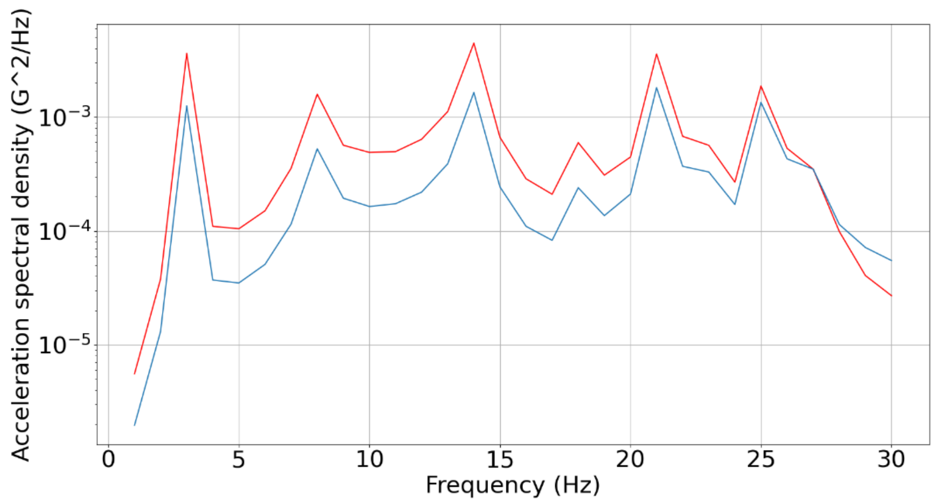

Figure 3-39: Stress PSD. Blue curve: for constant acceleration of 1mm/s2; Red: scaled with the PSD of the road.

3.5.3.3.2 Applying Dirlik's method

With the stress PSD of the component obtained, we can now apply Dirlik's method to estimate fatigue life. Dirlik's approach provides a semi-empirical expression to compute the probability density function (PDF) of the stress cycles, directly from the stress PSD. This bypasses the need to synthesize long time-domain signals — a clear advantage when dealing with complex structures and long-life predictions.

The main steps are as follows:

- From the stress PSD, compute its spectral moments:

$$m_n = \int_{f_{min}}^{f_{max}} f^n \; PSD(f) \mathrm{d} f,$$

  Where n is the order of the moment

- Calculate statistical parameters (not detailed here)
- Use Dirlik's empirical expression to obtain the PDF of stress ranges $p(s)$.
- Combine this PDF with the material's S-N curve (Wöhler curve):

$$N(S) = \left(\frac{S}{\sigma_0}\right)^{-1/b},$$

  Where $\sigma_0$and b are material constants.

- Finally, compute the expected damage per unit time using Miner's rule:

$$D = \int p(S) \frac{1}{N(s)} \mathrm{d} S$$

This damage rate D can then be scaled to estimate the fatigue life of the component under the assumed road excitation profile. It should be noted that several open source packages have already implemented these steps [29].

It must be stressed that the accuracy of the result depends both on the quality of the input PSD and the relevance of the material fatigue properties used (notably the S-N curve parameters). As road excitation is highly variable, one should always interpret these results as estimates for a specific road and usage scenario.

For this analysis, the material considered is a standard structural steel. The main fatigue properties of this steel — namely the endurance limit, the slope of the S-N curve, and other relevant parameters — are summarized in Table 3-13.

Table 3-13: Fatigue parameters of standard steel

Ultimate tensile strength σ_u	Yield Strength σ_y	Endurance limit σ_e	Slope of SN curve k	C
400 MPa	250 MPa	125MPa	4	8.1×10^{15}

Using the stress PSD computed previously (Figure 3-39) and applying Dirlik's method as outlined above, we estimate the accumulated damage under the given road excitation profile. The corresponding predicted fatigue life of the component — expressed in hours driven — is:

Estimated time before damage: **35 500hours**

In this example, the estimated fatigue life amounts to more than **40 years**, which is comfortably above the expected vehicle lifetime, confirming that the structural integrity of the mounting plate is adequate under the studied conditions. Of course, it is worth recalling that road-induced excitation is highly variable: harsher driving environments would reduce the predicted life, while smoother conditions would improve it. It is therefore recommended to repeat this analysis for several road classes to ensure robustness across different use cases.

While some may find 40 years for a steel plate a surprisingly short lifetime, this figure should be interpreted with caution for several reasons:

- the assumed PSD for the road is arbitrary and serves mainly as an example;
- we assumed a steel with relatively low stiffness to represent a worst-case scenario;
- 40 years is not a hard threshold beyond which the component becomes unusable — it is merely an estimate of when the first fatigue cracks could appear;
- the analysis was conducted on the mounting plate of the roof, which is not a perfectly planar component and contains local stress concentrations; the actual solar roof will have a smoother geometry, likely resulting in lower stress.

To obtain more reliable and accurate results, two key improvements would be necessary: first, the use of measured road profile data that reflects actual vehicle usage; and second, performing fatigue testing on a real or prototype solar roof to properly characterize its structural behaviour and validate the fatigue model parameters.

3.5.4 Conclusion on acoustics, vibration and fatigue analyses

In this study, a Finite Element Method (FEM) approach was used across all domains — acoustics, structural vibrations and fatigue — to model and analyze the behavior of the vehicle and its components under dynamic excitations.

For the acoustic part, a high-order FEM solver combined with an Adaptive Modal Expansion (AML) technique was employed. The acoustic excitation was modelled using a single monopole source, and reciprocity principles were leveraged to optimize computational cost. A simple mitigation solution was proposed: adding a carpet lining on a cavity surface, which was shown to significantly reduce noise between 600 Hz and 900 Hz.

For the structural vibration analysis, the full assembly was modelled with careful treatment of the connections (welds and bolted joints). By linking engine RPM to excitation frequency, it was possible to avoid solving the system at all frequencies, instead focusing on those most relevant to real-life operation.

Finally, for fatigue, a simple application of Dirlik's method was performed, based on the Power Spectral Density (PSD) of the maximum von Mises stress computed from road-induced vibrations. The component studied — the mounting plate for the solar roof — showed a satisfactory lifetime under the assumed conditions. However, to draw robust conclusions for more critical parts such as the actual solar roof, further experimental data (measured road profiles, material fatigue tests) would be required.

Overall, the presented workflow demonstrates a flexible and computationally efficient methodology to anticipate acoustic comfort, vibration behavior and fatigue life at an early design stage.

4. Conclusion

Deliverable D4.2 - Simulation Environment & Integration – detailed the development of the GIANTS simulation platform within Task T4.1 and provided an overview of the platform's capability to assess thermal and energy behaviour. Linking to T4.2, the effects of heat and NVH characteristics on the lifetime are also listed and described.

Specifically, Deliverable D4.2 demonstrates the integration of thermal, electrical, mechanical, and control-domain models into a unified co-simulation platform for adaptive energy management and end-of-life prediction in frugal electric vehicles. A key outcome was the implementation of a modular simulation environment, enabling real-time, IP-protected co-simulation across domains and component suppliers.

On the thermal modelling side, a physics-based 1D battery model was developed in Matlab Simscape, validated over ten realistic driving and charging scenarios. A complementary thermal model for the charging station was implemented, enabling dynamic cycling simulations by thermally switching between vehicle and charging states.

Battery lifetime modelling combined low-cost formulations for cycling and calendar aging, capturing key degradation phenomena (resistance increase, capacity fade) based on thermal and usage profiles.

Noise and vibration comfort was assessed using Finite Element Methods, enabling virtual evaluation of structural and acoustic performance. This approach helped identify critical transmission paths and supported lightweight NVH treatment strategies aligned with GIANTS' frugal design philosophy.

Together, these developments advance the state-of-the-art in predictive, cross-domain modelling for affordable, efficient EVs. The platform sets the foundation for future validation and design optimisation, while also supporting broader GIANTS objectives in digital twin deployment, lifetime extension, and energy-efficient transport and in particular into tasks T4.3-T4.4 and deliverables D4.3-D4.4.

5. Abbreviations

Please include any abbreviations, terms etc. used within the deliverable in alphabetical order.

Term	Definition
AML	Adaptive Matched Layer
BEM	Boundary Element Method
BIW	Body-In-White
BMS	Battery Management System
CAD	Computer Aided Design
CLTC	China Light-Duty Vehicle Test Cycle
DOF	Degree Of Freedom
FEM	Finite Element Model/Method
FMU	Functional Mock-up Interface
FRF	Frequency Response Function
GIANTS	Green Intelligent Affordable New Transport Solutions
MIDC	Modified Indian drive cycle
NVH	Noise, Vibration, and Harshness
OCV	Open Circuit Voltage
PML	Perfectly Matched Layer
PSD	Power Spectral Density
PU	Public
R	Document, Report
REB2	Rigid Element Beam 2-nodes
RPM	Revolution Per Minute
SOC	State Of Charge
VCU	Vehicle Control Unit
WLTC	Worldwide Harmonised Light Vehicle Test Cycle
WMTC	World Motorcycle Test Cycle
WP	Work Package

6. References

[1] M. Doyle, T. Fuller and J. Newman, “Modeling of Galvanostatic Charge and Discharge of the Lithium/Polymer/Insertion Cell,” *Journal of the Electrochemical Society,* vol. 6, no. 140, p. 1526, 1993.

[2] U. Chopra and N. Biju, “Real-World Aging Prediction of a Lithium-Ion Battery Using a Simulation-Driven Approach,” *SAE Technical Paper,* no. 2023-01-0508, 2023.

[3] Wurzenberger, Jelovic, Šimundić and Mele, *Battery Thermal Management Simulation - 1D+1D Electrochemical Battery and 3D Module Modeling on Vehicle System Level,* 2021.

[4] K. Maher, A. Boumaiza and R. Amin, “Thermal management challenges in lithium-ion batteries: understanding heat generation mechanisms,” *Chemical Communications,* 2025.

[5] J. Marcicki and X. Guang Yang, “Model-Based Estimation of Reversible Heat Generation in Lithium-Ion Cells,” *Journal of the Electrochemical Society,* 2014.

[6] V. Sangwan, R. Kumar and A. Rathore, “State-of-Charge estimation of Li-ion battery at different temperatures using particle filter,” *The Journal of Engineering,* pp. pp. 5320-5324, 2019.

[7] J. Vetter, P. Novák, M. Wagner, C. Veit, K.-C. Möller, J. Besenhard, M. Winter, M. Wohlenfahrt-Mehrens, C. Vogler and A. Hammouche, “Ageing mechanisms in lithium-ion batteries,” *Journal of Power Sources,* Vols. 1-2, no. 147, pp. pp. 269-281, 2005.

[8] P. K. Roy, M. Shahjalal, T. Shams, A. Fly, S. Stoyanov, M. Ahsan and J. Haider, “A separate simplified vehicle model calculates the current profile that is used for the simplified electric circuit, based on the different vehicle characteristics, such as weight, frontal area and tire radius. The vehicle model and electric circuit are u,” *Electronics,* 2023.

[9] J. Peters, “Modeling calendar aging in Li-ion batteries,” *Journal of Power Sources,* no. 360, 2017.

[10] P. M. Attia, “Review—“Knees” in Lithium-Ion Battery Aging,” *Journal of The Electrochemical Society,* no. 169, 2022.

[11] M. Alipour, C. Ziebert, F. Conte and R. Kizilel, “A Review on Temperature-Dependent Electrochemical Properties, Aging, and Performance of Lithium-Ion Cells,” *Batteries,* no. 6, 2020.

[12] A. Rammohan, Y. Wang, S. Kannappan, S. Kumar, B. Ashok, H. Kotb, K. AboRas and A. Yousef, “Service life estimation of electric vehicle lithium-ion battery pack using arrhenius mathematical model,” *Front. Energy Res.,* no. 12, 2024.

[13] M. Feinauer, M. Wohlfahrt-Mehrens, M. Hälzle and T. Waldmann, “Temperature-driven path dependence in Li-ion battery cyclic aging,” *Journal of Power Sources,* no. 594, 2024.

[14] S. S. Zhang, “A review on electrolyte additives for lithium-ion batteries,” *Journal of Power Sources,* no. 162, pp. pp.1379-1394, 2006.

[15] P. Keil, S. Schuster and J. Wilhelm, “Calendar Aging of Lithium-Ion Batteries,” *Journal of Electrochemical Society,* no. 163, 2016.

[16] W. Hua, S. Wang and M. Knapp, “Structural insights into the formation and voltage degradation of lithium- and manganese-rich layered oxides,” *Nature Communications,* no. 10, 2019.

[17] J. Qu, Z. Jiang and J. Zhang, “Investigation on lithium-ion battery degradation induced by combined effect of current rate and operating temperature during fast charging,” *Journal of Energy Storage,* no. 52, 2022.

[18] W. Europe, Environmental Noise Guidelines for the European Region, 2018.

[19] A. Ern and J. Guernond, Finite Elements II, springer.

[20] S. Brenner and L. Ridgway Scott, The Mathematical Theory of Finite Element Methods, Springer.

[21] H. Bériot, A. Prinn and G. Gabard, “Efficient implementation of high-order finite elements for Helmholtz problems,” *International Journal for Numerical Methods in Engineering,* 2015.

[22] J. Berenger, “A perfectly matched layer for the absorption of electromagnetic waves,” *Journal of Computational Physics,* 1994.

[23] H. Bériot and A. Modave, “An automatic perfectly matched layer for acoustic finite element simulations in convex domains of general shape,” *International Journal for Numerical Methods in Engineering,* 2020.

[24] W. Beyn, “An integral method for solving nonlinear eigenvalue problems,” *Linear Algebra and its Applications,* 2012.

[25] B. De La Hosseraye, H. Wang, F. Georgiou, M. Hornikx and P. Robinson, “Derivation of time-domain surface impedance boundary conditions based on in-situ surface measurements and model fitting,” in *International Congress on Acoustics*, Aachen, 2019.

[26] R. Lyon and G. Maidanik, “Power Flow Between Linearly Coupled Oscillators,” *Journal of the Acoustical Society of America,* 1962.

[27] T. Dirlik, “Application of computer in fatigue analysis - PhD thesis,” 1985.

[28] J. Vande Kamp, “Analyzing Field Environments to Understand Product Failure Causes,” [Online]. Available: https://vibrationresearch.com/resources/analyzing-field-environments-to-understand-product-failure-causes/.

[29] Ladisk, *FLife python package,* University of Ljubljana.